



BRNO UNIVERSITY OF TECHNOLOGY

VYSOKÉ UČENÍ TECHNICKÉ V BRNĚ

FACULTY OF MECHANICAL ENGINEERING

FAKULTA STROJNÍHO INŽENÝRSTVÍ

INSTITUTE OF PHYSICAL ENGINEERING

ÚSTAV FYZIKÁLNÍHO INŽENÝRSTVÍ

ANALYSIS AND CHARACTERISATION OF SPIRALLY- ARRANGED FIELD-EMISSION NANOSTRUCTURE

ANALÝZA A CHARAKTERIZACE SPIRÁLNĚ USPOŘÁDANÉ AUTOEMISNÍ NANOSTRUKTURY

BACHELOR'S THESIS

BAKALÁŘSKÁ PRÁCE

AUTHOR

AUTOR PRÁCE

Martina Ondříšková

SUPERVISOR

VEDOUCÍ PRÁCE

Ing. Alexandr Knápek, Ph.D.

BRNO 2022

Assignment Bachelor's Thesis

Institut: Institute of Physical Engineering
Student: **Martina Ondříšková**
Degree program: Physical Engineering and Nanotechnology
Branch: no specialisation
Supervisor: **Ing. Alexandr Knápek, Ph.D.**
Academic year: 2021/22

As provided for by the Act No. 111/98 Coll. on higher education institutions and the BUT Study and Examination Regulations, the director of the Institute hereby assigns the following topic of Bachelor's Thesis:

Analysis and characterisation of spirally–arranged field–emission nanostructure

Recommended bibliography:

TALIN, A. A.; DEAN, K. A.; JASKIE, J. E. Field emission displays: a critical review. Solid-state electronics, 2001, 45.6: 963-976.

HARRIS, J. R., et al. Shielding in ungated field emitter arrays. Applied Physics Letters, 2015, 106.20: 201603.

KOCH, Christian; RINKE, Titus J. Photolithography: Basics of Microstructuring. MicroChemicals GmbH, 2017.

LYSHEVSKI, Sergey E. Engineering and scientific computations using MATLAB. John Wiley & Sons, 2005.

Deadline for submission Bachelor's Thesis is given by the Schedule of the Academic year 2021/22

In Brno,

L. S.

prof. RNDr. Tomáš Šikola, CSc.
Director of the Institute

doc. Ing. Jaroslav Katolický, Ph.D.
FME dean

Summary

Cathodes containing arrays of high aspect ratio field emitters are of great interest as sources of electron beams for vacuum electronic devices. The desire to maximize current and current density leads to the design of denser arrays. However, denser arrays lead to undesirable field shielding effects caused by the presence of surrounding emitters in the array. To reduce the shielding effect and thus maximize the field enhancement, an array of emitters was designed with an arrangement inspired by the natural phenomenon of phyllotaxis. The structure thus designed was created using electron beam lithography and reactive ion etching to form micropillars. A black silicon etching technique was used to create ultra-sharp tips with a radius in the order of tens of nanometers on the top of each micropillar. Analysis of the sample topography was performed by Scanning electron microscopy. Ultraviolet photoelectron spectroscopy was used to determine the work function. To find out the emission properties of the fabricated structures, a Field emission microscope was constructed and its electron gun was modified to experimentally use the fabricated structure as the cathode. A Murphy-Good plot was used to analyze the field emission data, to which the orthodoxy test was applied to check the validity of the experimental I-V data. Current stability measurement was performed to observe current fluctuations.

Abstrakt

Katody obsahující pole emitörů s vysokým poměrem stran budí velký zájem jako elektronové zdroje pro vakuová zařízení. Ve snaze maximalizovat proud a proudovou hustotu byly navrženy hustší pole emitörů. To však vedlo k nežádoucím účinkům, jako je stínění pole, způsobené přítomností okolních emitörů v poli. Pro snížení efektu stínění, a tím pádem zvýšení proudové hustoty, bylo navrženo pole emitörů s uspořádáním inspirovaným přírodním principem fyloaxe. Takto navržená struktura mikropilířů byla vytvořena pomocí elektronové litografie a reaktivního iontového leptání. K vytvoření ultra ostrých hrotů s poloměrem v řádu desítek nanometrů na vrcholu každého mikropilíře byla použita technika leptání black siliconu. Analýza topografie vzorku byla provedena pomocí rastrovacího elektronového mikroskopu. Pro stanovení výstupní práce byla použita ultrafialová fotoelektronová spektroskopie. Pro zjištění emisních vlastností vyrobených struktur byl zkonstruován emisní mikroskop, jehož elektronové dělo bylo upraveno tak, aby vyrobená struktura sloužila jako katoda. Graf Murphy-Good byl použit k analýze dat o emisních vlastnostech, na které byl aplikován ortodoxní test pro kontrolu validity. Pro sledování fluktuací proudu bylo provedeno měření stability.

Keywords

Field emitter array (FEA), electron beam lithography (EBL), reactive ion etching (RIE), black silicon, scanning electron microscopy (SEM), ultraviolet photoelectron spectroscopy (UPS), field emission microscopy (FEM).

Klíčová slova

Pole emitörů, elektronová litografie, reaktivní iontové leptání, black silicon, rastrovací elektronový mikroskop, ultrafialová fotoelektronová spektroskopie, emisní mikroskop.

ONDŘÍŠKOVÁ, M. *Analýza a charakterizace spirálně uspořádané autoemisní nanostruktury*. Brno: Vysoké učení technické v Brně, Fakulta strojního inženýrství, 2022. 56 s. Vedoucí práce Ing. Alexandr Knápek, Ph.D.

I hereby declare that I wrote this bachelor's thesis on my own with a supervision of Ing. Alexandr Knápek, Ph.D., and all the literature used is listed in the references.

Martina Ondříšková

First of all, I would like to thank my supervisor Ing. Alexandr Knápek, Ph.D. Not only for his guidance and all the help but also for all the discussions over excellent coffee about physics and non-physics. Thank you for the opportunity to be part of the amazing E-Beam Lithography Group at the Institute of Scientific Instruments of the Czech Academy of Sciences.

I would like to thank all my colleagues from the Lithography group, namely Ing. Jakub Sadílek for his help in sample preparation and also for teaching me to be more independent, Mohammad Allaham, M.Sc., for his advice during the measurements and also his great help in processing the results, for his theoretical calculations and all the consultations, and Mgr. Daniel Burda for the XPS measurements and his advice. Last but not least, doc. Ing. Vladimír Kolařík, Ph.D., Ing. Milan Matějka, Ph.D., Bc. Jana Chlumská, and all the others. I am grateful for everything they taught me.

I'm beyond grateful to all the friends I have met thanks to studying physics, I never thought I could meet friends for life here.

Thank you so much, Kája, for being there for me all these three years and I hope you will always be there, I could never have done it without you.

Finally, I would like to give a special thanks to my family for being supportive and encouraging throughout my studies.

The research infrastructure was funded by the Czech Academy of Sciences project RVO:68081731.

CzechNanoLab project LM2018110 funded by MEYS CR is gratefully acknowledged for the financial support of the measurements/sample fabrication at CEITEC Nano Research Infrastructure.

Martina Ondříšková

CONTENTS

Introduction	3
1 Theoretical Part	5
1.1 Electron field emission	5
1.2 Field emission arrays	11
1.2.1 State of art	11
1.2.2 Orthogonal arrangement	16
1.2.3 Shielding effects	17
1.2.4 Nonorthogonal arrangement	18
1.3 Phyllotaxy	19
2 Sample fabrication	21
2.1 Distribution of emitters	21
2.1.1 Data	22
2.2 Lithography methods	23
2.2.1 Substrate preparation	24
2.2.2 Patterning with an electron beam	25
2.2.3 Resist development	26
2.2.4 Results	26
2.3 Etching techniques	27
2.3.1 Reactive ion etching	28
2.3.2 Deep reactive ion etching	29
2.3.3 Black silicon etching	30
3 Measurements and results	35
3.1 Sample topography	35
3.1.1 Scanning electron microscopy	36
3.1.2 X-ray photoelectron spectroscopy	37
3.2 Field emission microscope	40
3.2.1 Field emission imaging	41
3.3 Electrical properties	43
3.3.1 Ultraviolet photoelectron spectroscopy	43
3.3.2 I-V characteristics	44
3.3.3 Total emission current stability	47
Conclusions	49

References	51
List of symbols, quantities and abbreviations	55

INTRODUCTION

To understand the world at the nanoscale and to develop that understanding further, the desire to make things smaller and faster, and more powerful, requires advanced electron vacuum technologies. The key to these technologies for nanoscale exploration and fabrication is a free electron source due to its resolution.

The simultaneous field emission from multiple point emission sources has been the subject of investigation for the last 50 years and has given its potential advantages of cold-cathode and extended area electron sources for many important device applications. The key features of a field emission array are the highest current and current density, which can be achieved with denser arrays. However, when arrays are denser and the individual emitters are too close together, an undesirable field shielding effect occurs due to the proximity of the surrounding emitters.

To reduce the shielding effects of some existing field emission arrays and to increase the field enhancement, thus maximizing the total emission current, a natural phenomenon called phyllotaxis, the positioning of plant leaves and seeds on the stem is included. The beauty of nature is that it knows best how to arrange the leaves so that they are optimally positioned to absorb sunlight, capture raindrops and access the air and that due to angular displacement described by an irrational number—the golden angle.

The fabrication of structures of high aspect ratio field emitters with an arrangement resembling that of sunflower seeds will be presented in this thesis. Advanced lithographic techniques and reactive ion etching, also deep reactive etching by the Bosch method, will be used to fabricate the micro-pillars in the array. Ultra-sharp tips with a radius in the order of tens of nanometers will be formed on the surface of each micropillar using the black silicon etching technique. This part will aim to find the right parameters for the formation of high aspect ratio black silicon.

Subsequently, the samples produced will need to be analyzed with respect to their topography. Techniques such as scanning electron microscopy and confocal microscopy can be used for this purpose. X-ray photoelectron spectroscopy (XPS) will be used as a technique to determine the chemical composition and contamination on the surface of the sample. Ultraviolet photoelectron spectroscopy (UPS) will serve to determine the work function. The electrical emission properties of the produced structures will be investigated on a modified vacuum apparatus of the field emission microscope which is modified to use the produced auto-emission structure as the cathode. A scintillator

will be used to display the emission pattern. A Murphy-Good plot will be used to evaluate the I-V characteristics and an orthodoxy test will be performed. Finally, the stability of the current will be measured.

1. THEORETICAL PART

1.1 Electron field emission

The most essential thing in electron microscopy, surface analysis, electron-beam lithography, and electron-beam welding is the free electron source with suitable parameters. There are several electron sources but only some of them have required parameters to be used in these techniques.

The basic principle of electron emission into a vacuum is to supply the electrons with enough energy to overcome the potential barrier preventing them from escaping from the electron shell of the atom. The emission occurs when electrons overcome this energy barrier. In classical mechanics, the passage of a particle through a potential barrier is only possible when its total energy exceeds the height of the barrier. If the particle does not have sufficient energy to overcome the barrier, then the particle stops when it reaches the barrier and continues in the opposite direction. In quantum mechanics, however, there is a non-zero probability of a particle passing through a potential barrier even if the total energy of the particle is less than the height of the barrier. This phenomenon is called quantum tunnelling. This behavior of particles in quantum physics is due to the wave-particle nature of subatomic particles.[1]

The minimum energy that needs to be provided for an electron to escape from a surface of a material is called the work function, whose value slightly varies for particular material depending on the process of emission. More precisely, the electronic work function is the smallest possible energy required to extract electrons at the Fermi level from inside a solid to its surface. [1]

The Fermi energy is defined as the energy of the highest filled level in the ground state of the N electron system. The ground state is the state of the N electron system at absolute zero temperature. [3]

Fig. 1.1 shows a representation of the work function φ_M of the metal, which is equal to the energy difference between the Fermi level E_{FM} of the metal and the vacuum level E_0 , where the electron can be released completely out of the material. The work function is strongly influenced by the surface layer of the material. The presence of even a monolayer of contamination atoms or the occurrence of reactions on the surface (e.g. oxidation) can change the work function. Changes can be on the order of 1 eV.

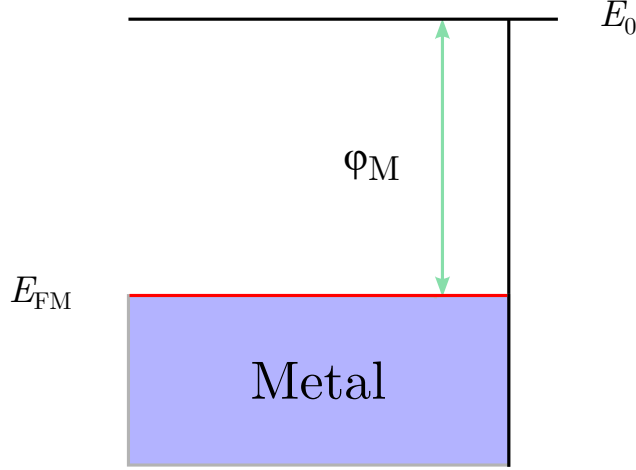


Figure 1.1: Band diagram illustrating work function in metal. Adapted from [2].

Types of emission are divided according to which kind of energy is provided to electrons. This is a phenomenon caused by the interaction of temperature and electric field.

The thermionic emission phenomenon is based on the thermal excitation of electrons in a solid. Energy spectrum of electrons at nonzero temperatures contains electrons at higher energy levels than the Fermi level. These electrons begin to contribute substantially into the emission current. An energy diagram illustrating this process is shown in Fig. 1.2. [4]

In the thermionic emission process, only those electrons are emitted from the cathode surface whose energy has risen to the energy level of free electrons in a vacuum by thermal action. Electrons with this energy can leave the emitter potential well. The emitted electrons are then extracted by the low electric field and thus gradually accelerated to the working energy.

The thermionic emission current density can be described by the Richardson-Dushman equation

$$j_T = A T^2 \cdot \exp\left(-\frac{\varphi}{k T}\right), \quad (1.1)$$

where A is Richardson's constant, T is the cathode temperature in K, φ is the electron work function in eV, and k is the Boltzmann constant. This equation applies to the conduction electrons in metals. [5]

Thermionic emission relies on heat to generate electrons by applying current to the hot cathode which can be metal filament or crystal. The filament is gradually heated until its electrons energy overcomes the work function of the material and escapes the solid surface. The charge flow magnitude increases with increasing temperature.

The filament source, in particular the tungsten wire, has the disadvantage that it gradually loses mass by evaporation of the material and eventually breaks. Another shortcoming is that due to the high temperature that must be applied to this source, lower brightness and broader beam spread is caused, which results in lower image reso-

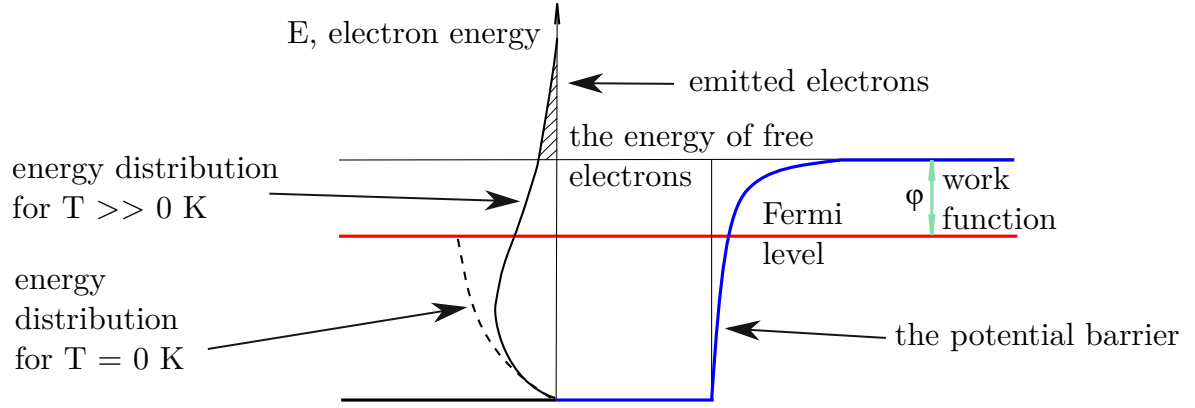


Figure 1.2: Energy diagram illustrating the thermionic emission process. Adapted from [5].

lution. As crystal source, lanthanum hexaboride (LaB_6) and cerium hexaboride (CeB_6) can be used, which consists of a single crystal of the respective molecule. Like tungsten fiber, crystals are heated by the applied current until there is not enough energy for electron emission. In comparison to the tungsten filament, a lower temperature is needed for the emission, which allows us to achieve lower beam spread and higher brightness. They are also less volatile, which significantly increases their service life compared to tungsten. Their downside is the need for a higher vacuum.

Within the field emission, the strong electrostatic field is applied to obtain electron emission at room temperature when the probability of occupation of the energy levels above the top of the potential barrier is zero. This process cannot be explained by means of classical physics. Electrons penetrate into the vacuum by quantum mechanical tunneling through a potential barrier at the metal-vacuum interface narrowed by a strong electric field. Electrons have a significant probability of tunneling from the solid into the vacuum. An energy diagram illustrating this process is shown in Fig. 1.3.

The Fowler-Nordheim equation describes the current density of field emission

$$j_F = \frac{k_1 E^2}{\phi} \cdot \exp \left(-\frac{k_2 \phi^{\frac{3}{2}}}{E} \right), \quad (1.2)$$

where E is the intensity of the electric field on the cathode surface, and k_1 , k_2 are constants. [5]

This phenomenon appear when the intensity of the electric field reaches values $1\text{--}3 \text{ V}\cdot\text{nm}^{-1}$. Emission occurs from the cathode surface at room temperature; a sharp tip of the tungsten wire is used as the cathode. The area from which the electrons are emitted lies in the nanometer range, which makes field emission area significantly smaller than in thermionic emission. Thanks to such a small emission area, it is possible

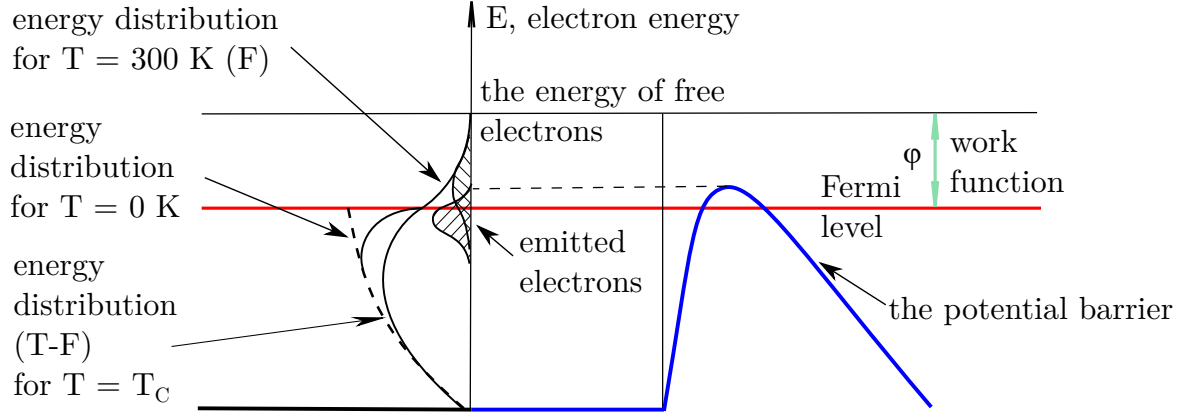


Figure 1.3: Energy diagram illustrating the field emission process. Adapted from [5].

to achieve excellent beam brightness and thus improved image quality, higher spatial resolution, and increased signal to noise. The benefit of these sources is also their long lifetime. Their main disadvantage is the cost of their use because an ultra-high vacuum is required for their operation. Another disadvantage is associated with fluctuation phenomena that occur in cathodes due to the impossibility of maintaining a chemically clean surface, as is the case, for example, with Schottky cathodes, where the surface is continuously cleaned due to the increased tip temperature causing evaporation of impurities.

There may be crossover between field emission and thermionic emission, where the two mechanisms intertwine. For field emission, we have to take into consideration the thermal stimulation of the field emission, and vice versa, for thermionic emission, we have to take into consideration the stimulation of thermionic emission by the electric field.

Field emission is not strictly temperature dependent at lower temperatures. As the temperature increases, excitation of electrons occurs. These excited electrons subsequently occupy even the energy levels just below the top of the potential barrier, an increase in current density occurs.

When the electric field on the surface of the emission structure is increased during the thermionic emission process, an increase in emission current is observed due to the deformation of the top of the potential barrier. This is reflected in a reduction of the work function ϕ . An energy diagram illustrating this process is shown in Fig. 1.4. Schottky explained this theoretically and described this phenomenon by a current density equation that contains correction terms

$$j_{FT} = A T^2 \cdot \exp\left(-\frac{\phi}{kT}\right) \cdot \exp\left(-\frac{\Delta\phi}{kT}\right), \quad (1.3)$$

where $\Delta\phi$ is the decrease in work function. [5]

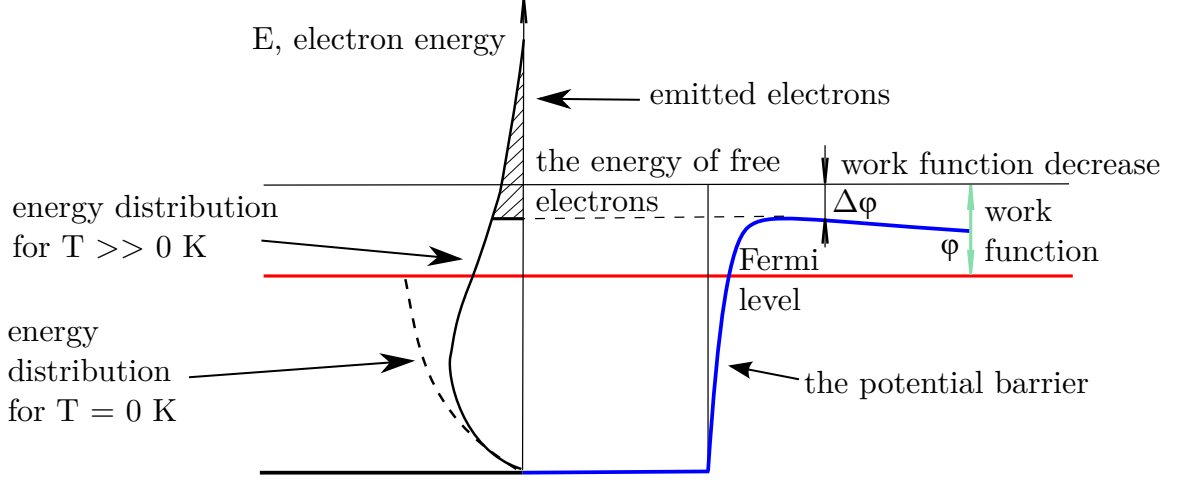


Figure 1.4: Energy diagram illustrating the field emission process with temperature influence. Adapted from [5].

By setting a higher temperature and lower electric field intensity at the cathode surface, the specific conditions under which Schottky emission dominates can be set. If the potential barrier is wide enough but the decrease in work function is already significant, then only the electrons from the immediate area around the top of the potential barrier can be emitted within a certain temperature range.

As already mentioned, Schottky emission is a type of field emission which is thermally assisted. The specific conditions of this type of emission are higher temperature and lower electric field intensity at the cathode surface. By applying electric field, the potential barrier is reduced and thermoelectrons are easily emitted. An energy diagram illustrating this process is shown in Fig. 1.5.

A part of the emitted electrons is emitted by the classical thermionic emission mechanism and a part by quantum tunneling through the top of the potential barrier, then the equation for the Schottky emission current density is

$$j_S = j_T \cdot \exp\left(-\frac{\Delta\phi}{kT}\right) \cdot \frac{\pi T_k}{2T} \cdot \sin^{-1}\left(\frac{\pi T_k}{2T}\right), \quad (1.4)$$

where j_T is the thermionic emission current calculated without the influence of the electric field, $\Delta\phi$ is the decrease in work function due to the electric field, and T_k is the temperature for which the maximum of the normal electron energy distribution is at the top of the potential barrier. [5]

It is therefore a type of emission in which the effects of temperature and electric field contribute about equally to the mechanism.

As Schottky source, the tungsten tip coated in zirconium oxide is used, which facilitates the thermionic emission of the electrons when the source is heated. Due to the thermal effects, Schottky emitters have a shorter lifespan than cold field emission sources and under certain conditions (e.g. lower voltage) they have a larger energy

spread. Although, their considerable advantage is a better stability.

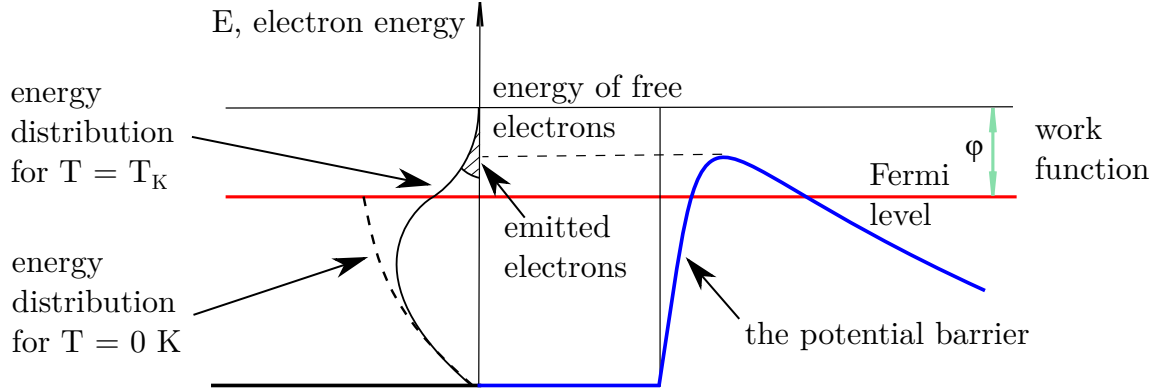


Figure 1.5: Energy diagram illustrating the Schottky emission process. Adapted from [5].

The band structure of semiconductors, unlike metals, contains a band gap. A band gap is a gap where no electronic states can exist. This band of energy is between the top of the highest filled band called the valence band E_V and the bottom of the empty band above it called the conduction band E_C . The width of the band gap is the main difference between semiconductors and insulators.

In the energy diagram of semiconductors, the Fermi level lies below the bottom of the conduction band. The Fermi energy is negative and usually less than 1 eV. The work function is the energy required to remove an electron from the Fermi level to the vacuum level. [6]

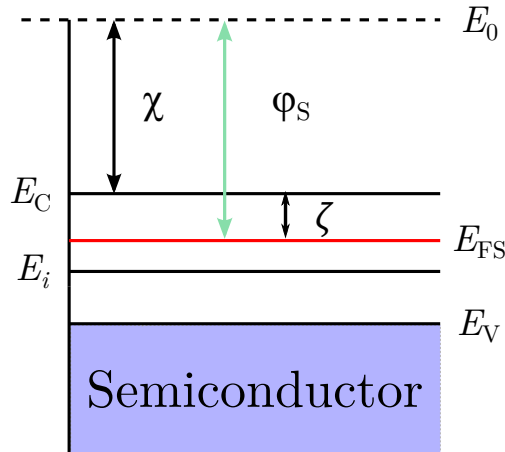


Figure 1.6: Band diagram illustrating work function in semiconductor. Adapted from [2].

Regarding the emission from the semiconductor, there may be both emission from

the conduction band and emission from the valence band. The probability of emission from the valence band depends on the width of the band gap.

Fig. 1.6 shows the energy diagram of a semiconductor and its work function φ_s which is equal to the energy difference between the Fermi level E_{FS} of the semiconductor and the vacuum level E_0 , where the electron can be released from the surface. E_C represents the bottom of the conduction band and E_V the top of the valence band. The negative Fermi energy ζ is equal to the distance between the Fermi level and the top of the conduction band. χ is the potential energy of the electrons in the conduction band and is given by [6]

$$\chi = \varphi_s + \zeta. \quad (1.5)$$

1.2 Field emission arrays

Electron field emission based on the principle of simultaneous emission from multiple individual emitters has been investigated for several reasons. Many important device applications take advantage of cold-field electron emission sources with extended-area capabilities. [7]

Planar electron sources have practical applications in displays, electron-beam lithography, ion propulsion/micro thrusters, information storage, and other devices. [8]

Advantages of field emission sources are such as generating high brightness electron beams which can meet the needs of particle accelerators, high power microwave, X-ray sources, and vacuum electronic devices. High current density is the result of quantum mechanical tunneling through an emission barrier the size of which is reduced by applying a strong electric field to the surface. [9]

1.2.1 State of art

Field emitter array cathodes as first introduced by Spindt et al. [10] in the late 1960s. They presented the fabrication and characterization of micron-size field emission tubes.

The emitters were conically shaped and placed under an extraction grid. The cathodes were formed into a sandwich on a sapphire substrate using thin film deposition (see Fig. 1.7). The sandwich was formed by a thin molybdenum-aluminum layer and a thin oxide-molybdenum layer. The "sandwich" had either regularly or randomly placed micron-sized cavities which contained a single molybdenum field emitting cone. Structures with an active area of about 10^{-3} cm^2 were formed with a random distribution of emitters. The geometry of the cones could be varied by adjusting the deposition parameters. Emission was obtained for applied voltages ranging from below 10 to about 200 V, which depended on the shape and length of the cones.

The others to follow up on fabricating field emission arrays in 1973 were Thomas et al. [7]. Until then, it was a challenge to make large-area emitters because of fabrication difficulties, such as exacting geometric uniformity that must be maintained on useful

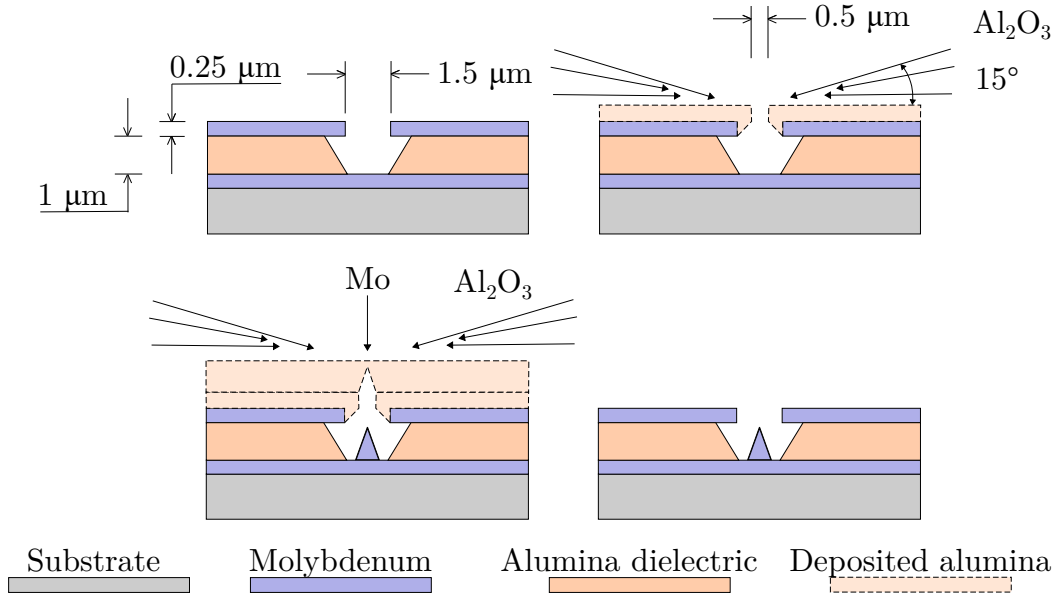


Figure 1.7: Cathode formation by deposition. Adapted from [10].

multiple emitter structures. Thomas et al. were the first to make large-area arrays up to 3 cm in diameter.

To fabricate patterns, they used photolithographic techniques. Geometrically uniform, relatively large structures were created using a rotational etching technique in which samples are etched in beakers that are tilted and slowly rotated. Very small tip dimensions of emitters in the 20 nm range have been achieved.

Two applications have been studied. First, it was presented that p-Si with a high resistivity is suitable for field emission photocathodes on which they demonstrated field emission imaging. The second application discussed was the use of n-Si emitter arrays which proved to be suitable for high-current cold-field emission cathodes. Total emission currents of 0.25 A from 1 cm² areas of 100 cm⁻¹ n-type emitters were achieved.

Spindt et al. [11], who first came up with field emitter array cathodes, carried on the research for high-current density applications.

An array of holes in the gate film and silicon dioxide layers were formed using lithographic techniques. Subsequently, molybdenum cones were formed in the center of these holes directly on the silicon substrate.

Cathode arrays were arranged in groups of 25 arrays on a single substrate, where each array includes from 1 to 10,000 emitters. The largest arrays cover an area of 1 mm in diameter and have tip-packing densities of up to $1.2 \cdot 10^6$ tips · cm⁻².

An attempt was made to achieve as high a packing density as possible, but this is limited by the etching process where there is a risk of cutting into neighboring holes. One way to increase the packing density is to increase the ratio of effective emitting area to the area occupied by the array. The other way that has been tried is to

create wedge-shaped emitters rather than point emitters. A comparison shows that the wedge configuration has more than 150 times the available emitting area than the tip configuration at the same number of wedges or tips. However, the disadvantage of the wedge configuration is a higher voltage to obtain the emission.

Emission tests were performed when a voltage of 1,200 V was applied to the collector. The field-emission cathode array development effort has shown that the emitter tips are in most cases capable of producing emission levels over 50 μA per tip. This at a cathode tip packaging density of $1.2 \cdot 10^6 \text{ tips} \cdot \text{cm}^{-2}$ corresponds to a current density of $60 \text{ A} \cdot \text{cm}^{-2}$. In several instances, tip loadings of over 100 μA per tip were measured with the same packaging density of $1.2 \cdot 10^6 \text{ tips} \cdot \text{cm}^{-2}$ corresponding to a current density of $120 \text{ A} \cdot \text{cm}^{-2}$. These values were only obtained with smaller arrays (less than 100 tips). However, at emission levels much greater than 20 mA (which is approximately $2.5 \text{ A} \cdot \text{cm}^{-2}$) voltage breakdown and destructive arcs are common. Larger arrays produce total current levels that exceed the capacity of the test apparatus. The lifetime of the cathodes produced exceeds 50,000 hours under controlled conditions.

Due to the considerable interest in vacuum microelectronics, designs for advanced device structures that use a cold cathode or field emitter array as the electron source have been developed.

Because of this interest, H. Lee and R. Huang [12] studied the field-emitter-array diode which has potential applications in applications such as flat screen displays and microsensors. Their work mainly studied the geometry of the emitters and their interaction between each other. The main geometrical parameters investigated are the distance between the tip and the collector, the radius of curvature of the emitter tip, and the distance between the two tips. It is found that as the distance between the tip and the collector is reduced, the interaction between the tips is lower and therefore the tips tend to behave as individual tips. Another parameter investigated that affects the behavior of the emitter array is the distance between the tips. The field strength at the tip decreases as the distance between the tips reduces, due to more interaction between the tips.

Significant design properties of the field emitter array have been found. The most striking one is that with the attempt to maximize the current from the field emitter array over a certain area, a limitation has been found regarding the density of the emitter array. This is due to the emitter-tip field strength lowering effect that is caused by the interaction between the tips. Another observation is that if we want to increase the field strength, we accomplish this by reducing the tip radius, but this is compensated by a reduced effective emitting area. In order to obtain the highest emitter current for a given design geometric parameters, it is required to determine the optimal tip radius.

Previous studies have mainly focused on the geometry of the emitter array and how the design can change parameters such as emission current, current density, and others. However, one of the important parameters is the voltage required for field emission. It is desirable to keep the voltage as low as possible. One way to achieve this is by

increasing the aspect ratio and sharpness of the emitters, which was investigated by McGruer et al. [13].

The structures were first formed by etching over a mask into SiO_2 . Subsequently, reactive ion etching was used to form silicon pedestals (1.8a). The silicon dioxide was then deposited by electron-beam evaporation (1.8b). Next, sharp tips were formed by the thermal oxidation of the silicon pedestals (1.8c). Self-aligned gates were formed by metal (in this case Al) evaporation. The last step was to remove SiO_2 and metal caps to reveal the emission tips (1.8d).

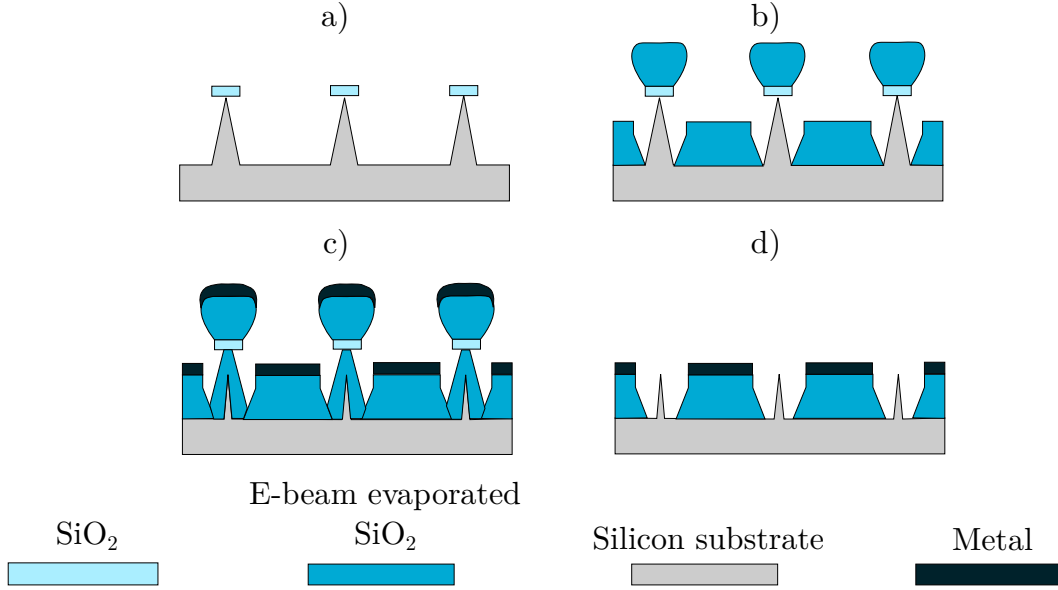


Figure 1.8: Self-aligned gated emitter fabrication process. Adapted from [13].

Emission tests were performed in an ultra-high vacuum chamber. The emission current of $25\ \mu\text{A}$ for a 300 emitter array is generally stable. The great advantage of these structures was that if the array exhibits a soft failure behavior, where an individual emission tip fails, the array as a whole continues to operate. Average currents of $0.3\ \mu\text{A}$ per tip in 1300-emitter arrays were achieved. The array has been demonstrated to continue operating stably for at least several hours.

Others who continued to try to achieve the smallest possible tip radius and thus reduce the turn-on voltage were Ding et al. [8] who achieved this with atomically sharp tips. Turn-on voltage in this context is defined as the gate voltage at which the emission current is $1\ \text{fA}$ per tip. Gate turn-on voltage is a critical parameter that is used to characterize the performance of field emission devices and its low value is desirable for the majority of field-emission array applications. Low turn-on voltage results in higher transconductance and lower input power consumption, it can also improve the burnout resistance and lifetime of the field emission array (FEA). The low turn-on voltage was achieved due to an atomically sharp tip which was fabricated by isotropic etching of silicon and low-temperature oxidation sharpening. The radius of curvature

less than 1 nm was achieved by repeated oxidation sharpening technique with turn-on voltage as low as 14 V.

A slightly different approach to fabricating micro and nanostructures used for field emission was shown by Johnson et al. [14] who formed a self-assembled silicon nanostructures using electron-beam rapid thermal annealing. They demonstrated the growth of nanowhiskers on n-type and p-type silicon substrates initiated by decomposition of the native oxide layer. The small radius of curvature of nanowhiskers is ideal for field emission. The structure thus formed demonstrated stable and repeatable emission behavior for fields as low as $2 \text{ V} \cdot \mu\text{m}^{-1}$. At the higher field, current saturation effects appear when no current increase can be achieved with a further voltage increase. These effects occur for both n-type and p-type samples, indicating that the mechanism affecting current saturation at high fields acts independently of substrate conduction type.

Back in 1990, H. Lee and R. Huang [12] observed that there is a certain dependence between the field strength at the tip and the distance between tips due to interaction between them. They discovered an emitter tip field lowering effect with the shortening of the distance between the emitters.

This was continued by Harris et al. [15] due to the effort to maximize current and current density. As mentioned above, higher current and current density can be achieved using a denser array, but for ungated emitters denser array leads to increased shielding. The microscopic geometry of emitters provides regions of local field enhancement. This allows emission to occur at much lower applied field strengths but localizes the emission to a small fraction of the cathode surface. The ratio of the enhanced local field to the background field is referred to as the field enhancement factor γ . If only a single tip is considered, γ increases primarily as a function of the emitter aspect ratio. In denser arrays where there is an increase of shielding effects the field enhancement factor γ of each emitter is reduced due to the presence of the other emitters in the array.

Shielding was found to be negligible if the distance between the emitters is greater than the emitter height for the two-emitter array. For large arrays, shielding is negligible if the emitter spacing is about 2.5 times the emitter height.

Further efforts to maximize the current and current density continued with simulations by Bieker et al. [16]. Work was focused on a large-area field electron emitter. They searched for the ideal spacing of individual emitters so that average emission current density and total current were maximized. Electrostatic depolarization effects, where polarization occurs due to induced charges on the surface caused by the application of an external field, were also considered.

Using the finite element method, it was investigated how to achieve ideal spacing with randomly distributed emitters. The method is based on the principle of finding the apex field enhancement factor and the specific emission current for an emitter as a function of the average distance of the nearest neighbor emitter. Simulations and modeling have shown that, as for regular emitter arrays, the optimal spacing for random

emitter arrays is also dependent on the value of the applied macroscopic electric field, to obtain maximum average current density.

Field emitter arrays have the advantage compared to single emitting sources that current fluctuation is reduced, maximum current and lifetime are enhanced. To improve the lifetime of the cathode, Edler et al. [17] used p-type semiconductor for field emitter array. An integrated current limiter was implemented for enhancing the lifetime and also because the local individual current limitation can lead to a more homogeneous current distribution over the array in the saturation region.

The origin of the current saturation of p-type silicon emitters was investigated because the operation in the current saturation region shows small current fluctuations, decreased degradation and thus an increased lifetime.

The change in the emitter surface was experimentally demonstrated. Furthermore, it is shown that there is a small voltage drop due to field penetration. Field penetration also results in a reduction of the field enhancement factor which is highly dependent on the geometry of the emitter array.

Measurements and simulations have shown that the origin of the current saturation level of a p-doped field emitter is strongly influenced by the reduction in the field enhancement factor which is caused by the change in the effective emission geometry due to field penetration. Also, surface generation and temperature have a great influence on the current saturation level. The current saturation level can be increased by surface modifications away from the apex. Further, by making certain changes in the design geometry, it may be possible to work at a higher temperature.

1.2.2 Orthogonal arrangement

Over the years, mostly either randomly arranged or orthogonally arranged field emission arrays have been developed. Orthogonal emitter geometries have been widely used in field emission displays, electron sources and other electronic devices.

Field emission is described theoretically by Fowler and Nordheim [18], who developed a general model for electron emission from planar surfaces, and their model is widely used to describe emission from large areas. [19]

The main requirements for field emitter arrays are low turn-on field, high current density, and good current stability. Lithographic techniques were used to fabricate patterns that fulfill these requirements. Sharp tips with high aspect ratios were fabricated by isotropic etching, where the parameters of this etching process allow to control the radius of curvature and aspect ratio of the tip.

A very suitable material for emission nanostructures is silicon due to its excellent field emission properties. This semiconductor material also has the advantage of a tunable energy gap and a controllable concentration of charge carriers.

Field emission performance depends on both the high aspect ratio and the sharp tip of the emitter. But there is also a strong dependence of the field strength at the tip on the distance between the emitters and their interaction with each other.

As a result of the interaction between the emitters, there is an emitter tip field strength lowering effect. Due to this effect, there is a limitation in the density of the emitter array. There is a way to increase the field strength by reducing the tip radius, however, this is compensated by reducing the effective emitting area. In denser arrays where there is more interaction between the emitters, there is also a reduction in the field enhancement factor γ of each emitter.

1.2.3 Shielding effects

In an attempt to get the highest current and current density, denser arrays were designed, however for ungated emitters, this results in an increased shielding effect. When the shielding effect occurs, it means that the field enhancement factor γ of each emitter is reduced due to the proximity of the other emitters in the array.

A method has been developed which models high aspect ratio emitters using tapered dipole line charges. This method is used to investigate the proximity effects of emitters in an array at any given distance from each other.

The shielding effect is a function of the array design geometry. The reduction in the field enhancement factor due to shielding is a function of the distance between the emitters.

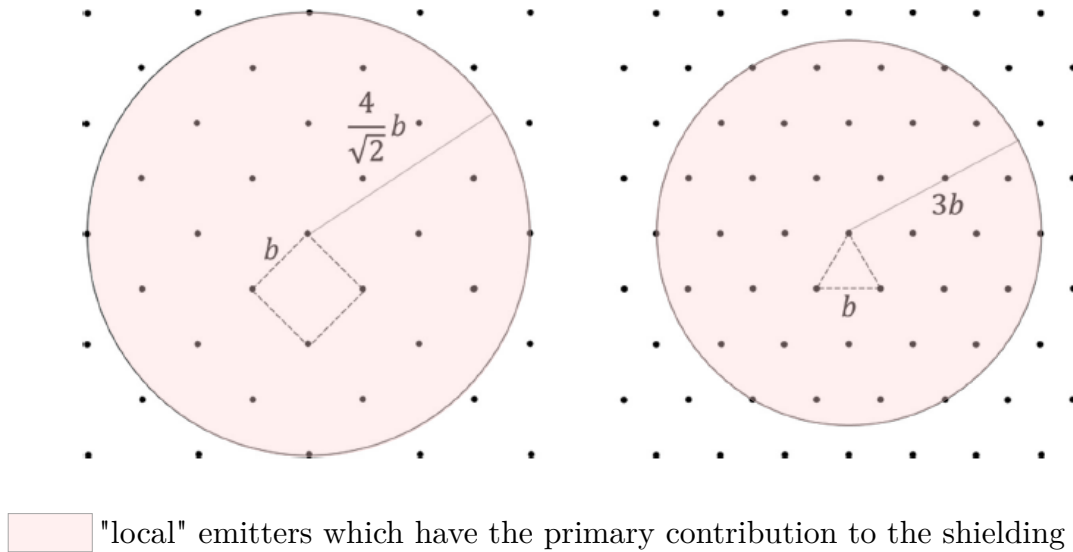


Figure 1.9: Square and triangular arrays, circles define the "local" area. Adapted from [15].

As mentioned earlier, shielding is negligible if the emitter spacing is greater than the height of the emitters for a two-emitter array. For larger arrays, the emitter spacing must be approximately 2.5 times the emitter height. A comparison of square and triangular arrays shows that the onset of shielding occurs at approximately the same time. However, triangular arrays have more than twice the emitter density as square

arrays for the same emitter spacing, so they are preferred for high current density field emission cathodes. Coulomb's law implies that the influence of one emitter on another must decrease with increasing the distance between them. This means that only some surrounding emitters must be considered when investigating shielding.

The main contribution to shielding in large arrays is made by "local" emitters at distances up to three times the spacing between the tips for both square and triangular emitters (see Fig. 1.9). From modelling and calculations, the distance of the surrounding emitters that still contributes to the shielding was found to be $4 \cdot \sqrt{2}$ of the distance b between the emitters for the square array and $3b$ for the triangular array. From the Fig. 1.9 it can be seen that for triangular arrays the emitter density is significantly higher. [15]

1.2.4 Nonorthogonal arrangement

Although the orthogonal arrangement has many applications in modern technology and its emission properties can be further improved, this may also reach its limits. Either a material limit or a limit in fabrication.

A different way to approach the fabrication of nanostructures is based purely on nature. The position of the elements is arranged like the position of seeds in a sunflower head. This arrangement of seeds on pseudanthium is a biological phenomenon known as phyllotaxis.

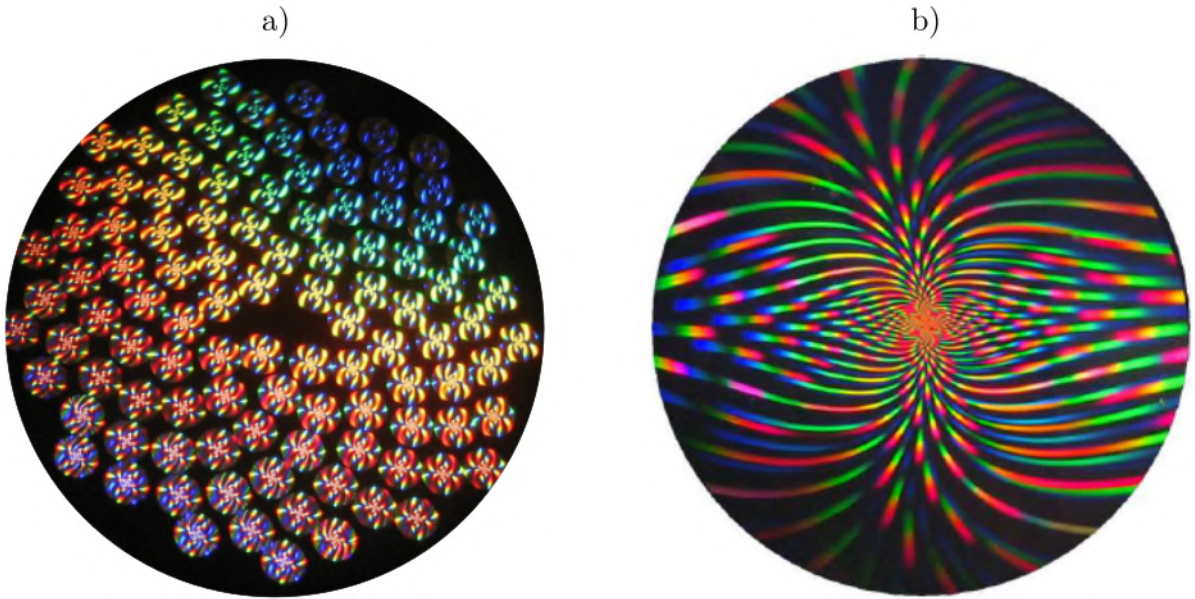


Figure 1.10: Diffractive pattern of the planar optical phyllotactic arrangement, a) [20], b) [21].

A design with this distribution has been used for example for optical elements (see Fig. 1.10) that show interesting properties and behavior in terms of reflection, refraction, and absorption at the nanometer scale. [21]

Another use of phyllotactic arrangement may be the design of an integrated circuit within the microelectronics field that contains an extensive number of pins. Analysis has shown that this arrangement can provide lower stress caused by thermal expansion in comparison to the classical orthogonal arrangement of pins. Fig. 1.11 shows a comparison using a numerical model which describes the thermal flow in the package. [21]

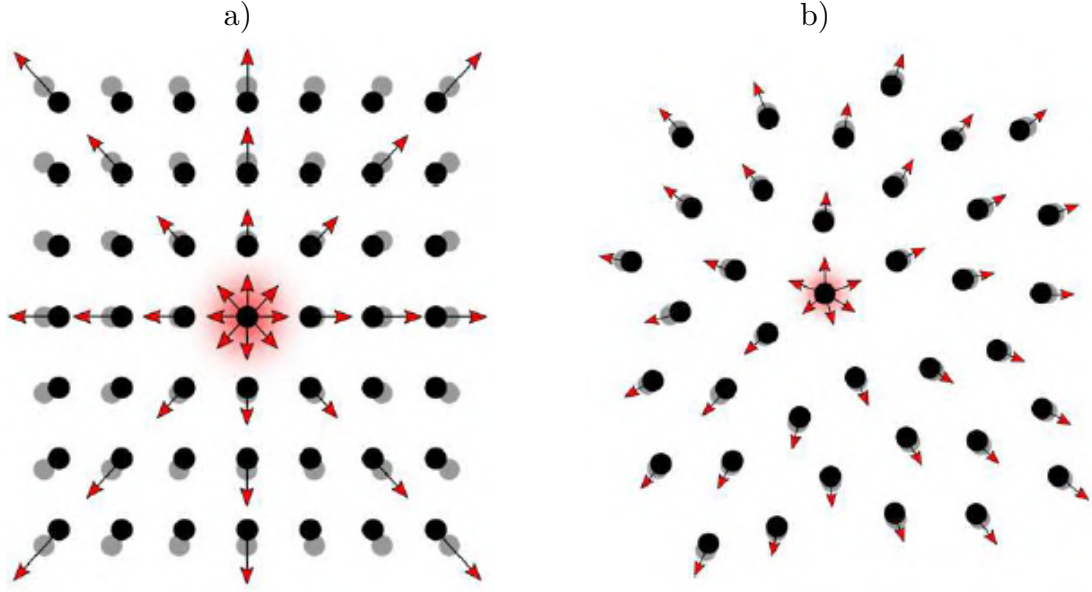


Figure 1.11: Heat distribution within a) orthogonal package, b) non-orthogonal arrangement based on the phyllotactic model [21].

This analysis, which shows a significant reduction of stress caused by thermal expansion of the integrated circuit within the microelectronics for the phyllotactic arrangement, suggests that applying this arrangement to a field-emission array could reduce the shielding effect caused by the proximity of the individual emitters to each other.

1.3 Phyllotaxy

Phyllotaxis is a phenomenon that originated in nature, describing the position of leaves and seeds of plants on the stalk. The phyllotactic model describes the arrangement of plant seeds. From a biological point of view, leaves grow in a way that is optimally adapted to absorbing sunlight, capturing raindrops, and accessing the air.

From a mathematical point of view, the distribution of the individual elements can be observed, given by the proportion of the terms of the F_n/F_{n+2} Fibonacci sequence, where the numerator is the number of cycles of the stalk and the denominator is the number of leaves on the generic spiral.

Vogel's mathematical model describes the arrangement of the seeds of a sunflower,

where the position of the elements is determined in the polar coordinates r and φ as

$$\{r_k; \varphi_k\} = \{c \cdot \sqrt{k}; k \cdot \varphi_0\}, \quad (1.6)$$

Where k is the order in the sequence of elements, c is the coefficient that determines the density of filling the region, and φ_0 is the angular constant. [22]

The individual elements, the seeds, lie on two arcs, one running clockwise and the other anti-clockwise. Their number in each set is always a member of the Fibonacci sequence 1, 1, 2, 3, 5, 8, 13, 21, . . . ; up to 233 for a big sunflower head. These arcs are not basic structural elements but are part of a single primary growth spiral.

The elements lying on the spiral have an angular displacement equal to the golden angle, which is obtained by dividing the full 2π (360°) angle into two parts α and β according to the golden ratio. The angles are obtained in the ratio

$$\frac{2\pi}{\alpha} = \frac{\alpha}{\beta}. \quad (1.7)$$

From which the β angle can be expressed as

$$\beta = 2\pi - \alpha. \quad (1.8)$$

Where, after adjustment and simplification, angles are equal to

$$\alpha = \pi(\sqrt{5} - 1) \doteq 222.5^\circ, \quad (1.9)$$

$$\beta = \pi(3 - \sqrt{5}) \doteq 137.5^\circ. \quad (1.10)$$

The golden angle is the smaller of the angles, i.e. the β angle.

The presence of the golden angle in the distribution of elements can be related to the concept of irrational numbers. The primary role of the elements (the specific case of leaves on the stem will be considered) is the interception of solar radiation and the intensity of photosynthesis which is proportional to the area of the leaves on which the solar radiation falls. The position of the leaves should therefore maximize this area. If the angle of leaf displacement on the stem corresponds to an irrational number, then no other leaf can be in exact overlap with a lower leaf as it rotates in a circle.

2. SAMPLE FABRICATION

2.1 Distribution of emitters

The distribution of individual emission elements (see Fig. 2.1) is inspired by a phenomenon from nature called phyllotaxis. The individual elements are distributed on a general spiral and their exact position, which I have plotted in python, is described by the following equations

$$\varphi = \frac{\sqrt{5} - 1}{2}, \quad (2.1)$$

$$\rho = (0 : n - 1) \cdot \pi, \quad (2.2)$$

ρ is the distance of the emitter from the center of the spiral, n is the number of elements.

Angular distance of the elements θ , which is relative to the angle $2\pi \cdot \varphi$. Angle $2\pi \cdot \varphi$ is obtained after dividing the full angle 2π in two parts according to the golden ratio. Angular distance of the elements is described as

$$\theta = (0 : n - 1) \cdot 2\pi \cdot \varphi. \quad (2.3)$$

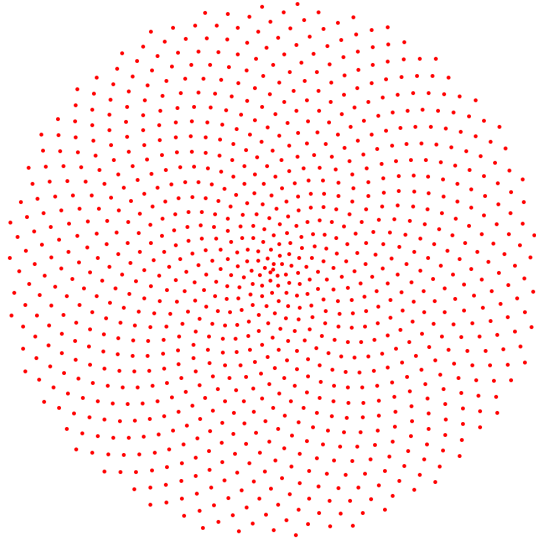


Figure 2.1: Distribution of emission elements.

Several designs of the final structures were created, where the angular distance always remained the same, only the number of elements n was changed. The final design contained structures with $n = 1,000$, $n = 2,000$, $n = 5,000$ and $n = 10,000$ (see Fig. 2.2). Structures with different numbers of elements were created in order to subsequently compare the emission behavior with the density of the active emitting area, the number of emitters per unit area.

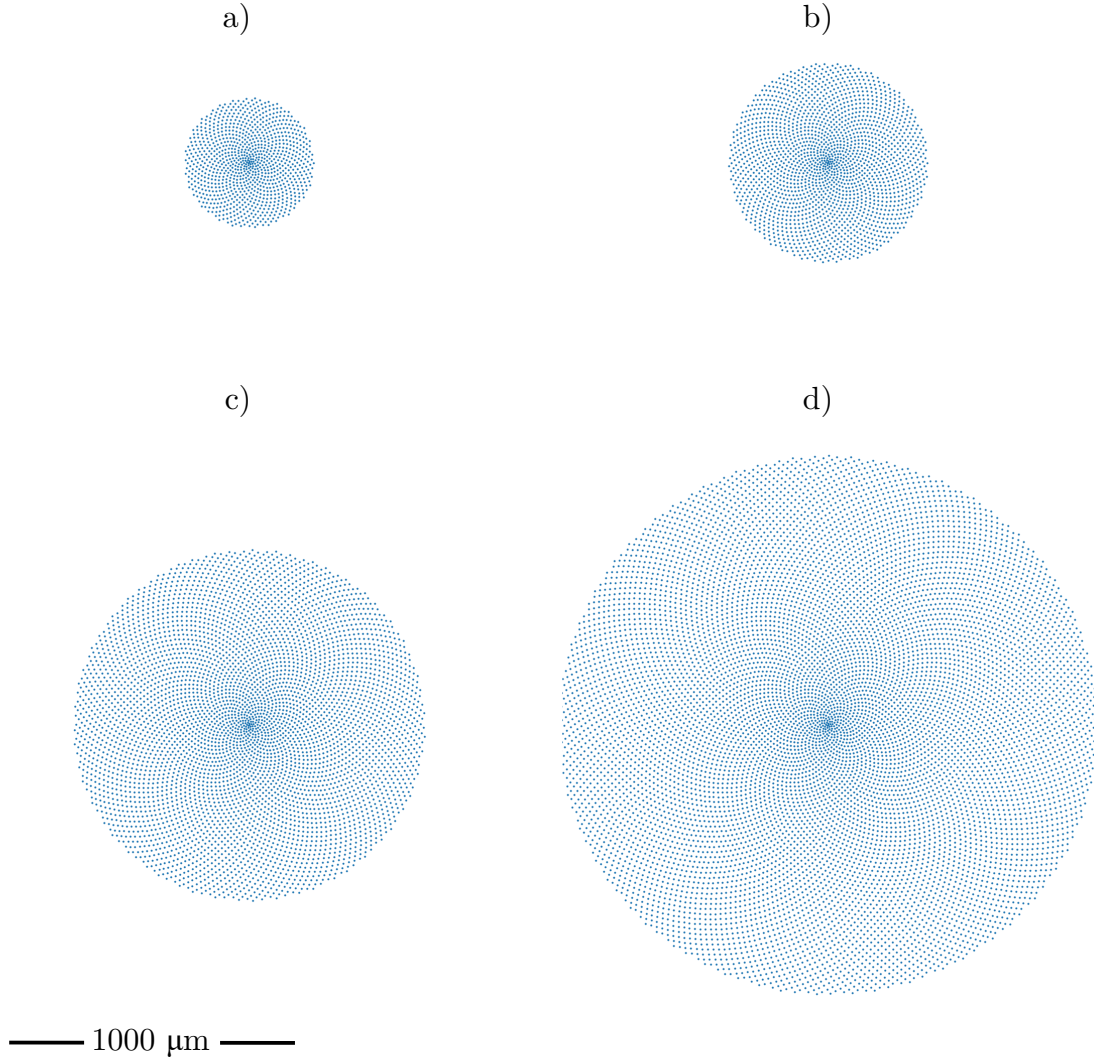


Figure 2.2: Design containing structures with a) $n = 1,000$, b) $n = 2,000$, c) $n = 5,000$ and d) $n = 10,000$.

2.1.1 Data

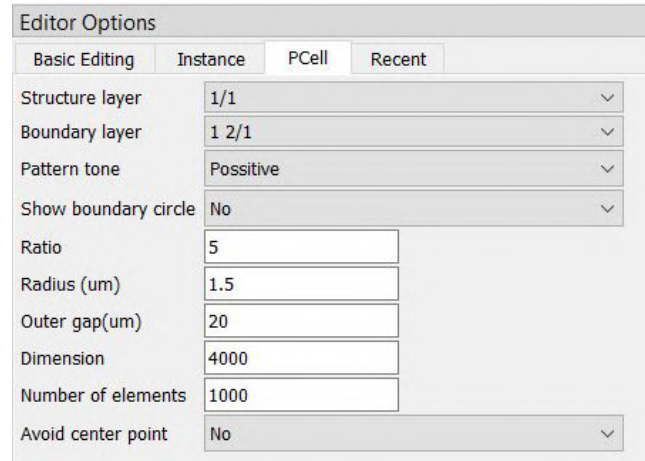
To create a motive, it is necessary to describe or somehow digitalize the motive to explicitly determine which parts of the resist are to be exposed.

To create a 2D design (layout), we can create motives using various software. The most suitable format for creating lithographic designs is Graphic data system (GDSII) or OASIS. To view and edit files in this format, GDS file Editor Software is needed—KLayout was used in this work. In this software, it is possible to view the layout, but also the individual layers of the pattern (for example if the lithography is done in multiple steps).

KLayout supports several design flows that can be mixed according to the project. The most common approach is to use the graphical user interface (GUI) to design using a library of fixed and parameterized cells. [23]

A PCell or parameterized cell is the basic building block for creating a design. It is created by entering parameters. The resulting motive includes dozens of such PCells and its creation involves up to hundreds of steps. Therefore Python scripts were used to create the motive, where the parameterized cell can be defined.

After running the Python script, a PCell was created, in this case, a defined spiral. In practice, several defined PCells are inserted on the resulting layout to cover the whole substrate—the wafer, and only their parameters are modified in the program as shown in the Fig. 2.3. The emitter radius, the number of elements n and other geometry parameters can be adjusted.



Editor Options			
Basic Editing	Instance	PCell	Recent
Structure layer	1/1		
Boundary layer	1 2/1		
Pattern tone	Positive		
Show boundary circle	No		
Ratio	5		
Radius (um)	1.5		
Outer gap(um)	20		
Dimension	4000		
Number of elements	1000		
Avoid center point	No		

Figure 2.3: PCell parameter adjustment in KLayout.

2.2 Lithography methods

Micro and nanolithography is a technology used to create patterns with a feature size in the range of a few nanometers to tens of millimeters. High-resolution topography with micro or nanoscale structures can be produced using a combination of lithographic techniques and other methods of fabrication such as deposition and etching.

Lithography can be divided into two types, depending on whether the electron beam exposure is through a mask—masked lithography, or whether direct spot-by-spot electron beam writing is performed—maskless lithography. The masked lithography uses

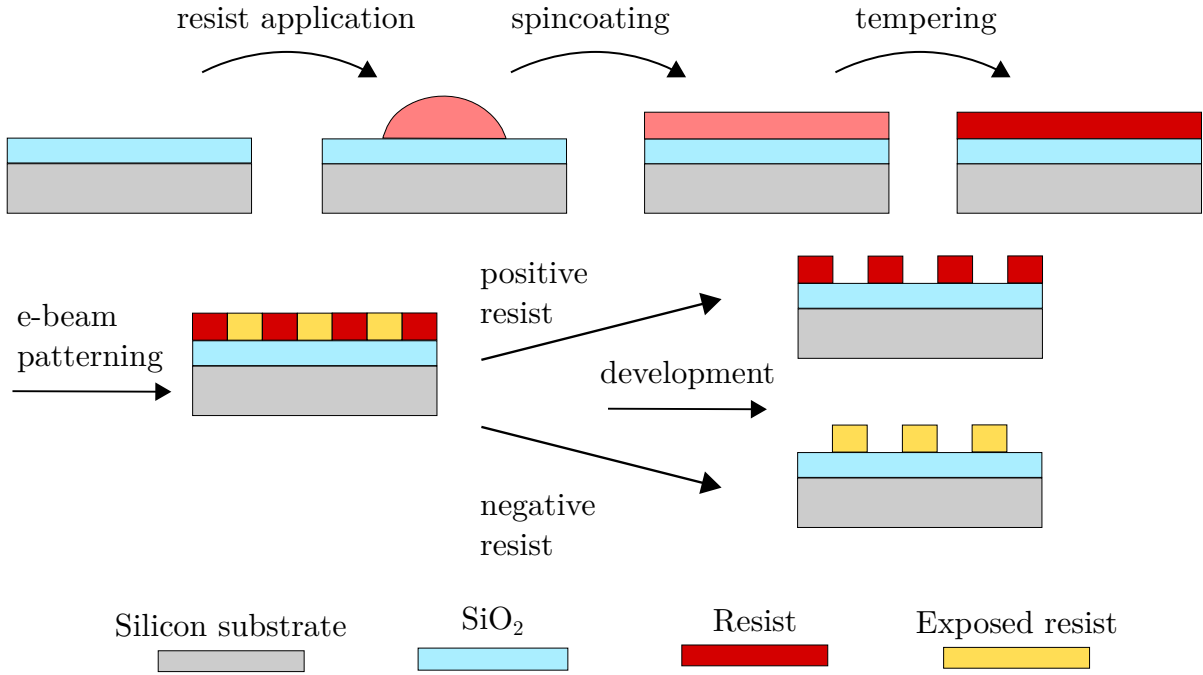


Figure 2.4: Individual processing steps in electron beam lithography.

a mask to transfer patterns over a large area. While this type of lithography does not have as high resolution, it has the advantage of the speed of writing. The forms of masked lithography include photolithography, soft lithography, and nanoimprint lithography. The maskless lithography produces arbitrary patterns with ultra-high resolution using direct writing. The minimum feature size is on the order of a few nanometers. However, the high resolution is compensated by the length of the patterning. The individual process steps of maskless electron beam lithography are shown in Fig. 2.4, they will be described in more detail in the following sections.

2.2.1 Substrate preparation

For the samples in this thesis, a boron p-doped silicon wafer for 1–5 Ω is used as the substrate. The silicon dioxide was thermally grown on the substrate to final thickness of 350–365 nm. The final thickness was measured using reflectometry or spectroscopic ellipsometry.

Heating the substrate for the desorption of water is part of the preparation of the substrate for the resist coating. For a clean substrate, it is recommended to perform a bake out at approximately 120 °C for a few minutes for the desorption of water molecules which are mostly adsorbed onto the surface.

An adhesion promoter was used to ensure proper adhesion of the resist to the substrate. The substrate is inherently hydrophilic after exposure to atmospheric humidity,

thus showing poor affinity with photoresist molecules. The adhesion promoter, in this case, HMDS (hexamethyldisilazane), is therefore used to make the substrate hydrophobic, water repellent, and thus photoresist-attractive. A layer of HMDS is applied on the heated substrate from the gas phase.[24]

The next step is to apply an electron beam resist, a thin layer of polymer solution sensitive to electron beam exposure. There are two types of resist, depending on what chemical reaction occurs after exposure with the electron beam.

In the case of a positive resist, a degradation process occurs upon exposure to electrons, producing polymer fragments with a lower molar mass. These exposed areas are soluble in the developer and, therefore, a positive exposure image is formed in the resist.

In the case of a negative resist, exposure electrons cause crosslinking processes, the exposed resist molecules form a three-dimensional network so that the molar mass of the polymer increases at the exposed area. By the action of a suitable developer, the unexposed polymer is solubled and a negative exposure image is formed in the resist layer. [25]

Resist deposition is performed using a spin coating technique, where a small amount of resist is deposited in the center of the substrate, which is then rotated to spread the resist layer into a uniform film by centrifugal force. By adjusting a certain spin speed, the thickness of the resist layer can be influenced. The thickness of the deposited layer is also influenced by the density of the resist.

After the coating, there is a residual solvent in the resist film, the amount of which is influenced by the type of resist and the thickness of the applied layer. Therefore, a soft bake must be performed to reduce the residual solvent. This process needs to be done for several reasons, such as to avoid contamination of the mask, improve the resist adhesion to the substrate, minimize the dark erosion during development, prevent defects during the process such as bubbling, and many others.

2.2.2 Patterning with an electron beam

In this work, the transfer (writing) of the image to the resist is performed by direct exposure with an electron beam in an electron beam lithograph, and in the second lithographic step, the laser direct writing method is used.

In electron beam lithography, the exposure can be performed in several ways. Exposure with a circular or Gaussian electron beam of constant or variable size, or writing with a rectangularly shaped beam of constant or variable size. The minimum size of the beam determines the possible resolution parameter of the device while the current density determines the writing speed parameter of the device. In the case of laser direct writing, the laser sequentially exposes the photoresist film on a direct path pixel by pixel.

Depending on the type of resist and the thickness of the resist layer, the required dose of electrons needed to change the polymer structure must be determined. The

required dose Q is described by the equation

$$Q = I \cdot t, \quad (2.4)$$

where I is current density of the beam and t is exposure time.

To change the dose, it is only necessary to vary the beam exposure time on the resist with a constant current in that beam. The equation also describes a very important parameter: the rate of exposure. The exposure rate is usually expressed in terms of the time required to expose (write) an image of a unit area of 1 cm^{-2} in a resist of a given sensitivity.

2.2.3 Resist development

After the exposure, it is sometimes preferable to do a baking step of the resist film which is called a post-exposure bake (PEB). For a normal positive resist, the reaction with the exposure is completed. Chemically amplified photoresists need a subsequent baking step. The PEB completes the photoreaction initiated during exposure.

Electrons or photons exposure of the resist creates a latent image of the transmitted image information in the resist layer. The development process induces this latent image by forming spots with or without resist. The development process involves the dissolution of macromolecular polymeric substances in a suitable solvent which is referred to as a developer.

2.2.4 Results

The samples were prepared on a $525\mu\text{m}$ thick silicon substrate on which a SiO_2 layer of $350\text{--}365\text{nm}$ thickness was coated by thermal oxidation. The wafer with the coated SiO_2 layer was subsequently coated with an approximately $3\mu\text{m}$ thick layer of AZ ECI 3027 for subsequent cutting. It was pre-cut from the backside into individual $(8\times 8)\text{mm}^2$ chips using an Oxford Laser A-Series laser cutter so that they could be broken apart at the end of the fabrication process. After the pre-cutting, the substrate was cleaned and the protective resist layer was taken off, which was done using N-methylpyrrolidone and then an ultrasonic methanol bath was performed to finish cleaning.

Before applying the resist layer, the sample was cleaned with oxygen plasma using Diener electronic NANO Plasma cleaner. It was then spin-coated with high contrast e-beam positive resist AR-P 6200.13 with an approximate thickness of 700 nm at 500 rpm for 5 s and then 1500 rpm for 60 s with an acceleration of 500 rpm/s . After this, the sample was then baked on a hotplate at 150°C for 60 s to allow the resist to harden.

For e-beam patterning, a Vistec EBPG5000plusES electron beam lithograph by Raith was used. The acceleration voltage of the electrons in the beam was 100 kV and the beam carried a current of 60 nA . The exact parameters of the electron beam are the spotsize of approximately 48 nm and the stepsize in x,y $(25\times 25) \text{ nm}$. The patterning dose was $330 \mu\text{C} \cdot \text{cm}^{-2}$.

Development was carried out using a AR-P 600-546 developer (amylacetate) for 75 s and then the sample was rinsed in deionized water. This prepared the pattern in the resist for subsequent reactive ion etching which is described in section 2.3.1, and also deep reactive ion etching which is described in section 2.3.2.

Subsequently, a second lithographic process was needed to cover the surrounding substrate so that the black silicon etching would only take place on the formed structures and not on the whole chip.

The substrate was vapour transported with the adhesion promoter HMDS at 130 °C in three cycles for 15 s and the subsequent reactions for 45 s. It was then spin-coated with high-resolution positive photoresist AZ ECI 3027 to an approximate thickness of 3 μm . The sample was then baked on a hotplate at 100 °C for 60 s to allow the resist to harden. For patterning, a direct-write photolithography machine MicroWriter ML3 Baby Plus by Durham Magneto Optics with patterning dose $240 \text{ mJ} \cdot \text{cm}^{-2}$ was used. Developing was done using an AZ 726 MIF developer for 60 s and then the sample was rinsed in deionized water.

The last processing step before black silicon etching, which is described in section 2.3.3, is the removal of the remaining oxide on top of the lithographically formed pillars. The oxide removal was performed using a BOE (See Fig. 2.7b)) (buffered oxide etch, also known as buffered HF – wet etchant) 7:1 which etches at approximately 70 nm per minute for 5 min 30 s at 22 °C. Subsequently, the sample was rinsed in deionized water.

2.3 Etching techniques

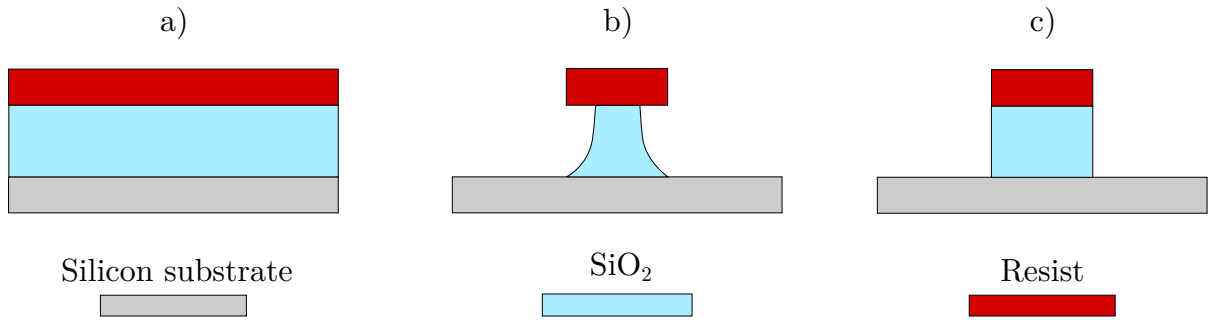


Figure 2.5: Profiles achieved by different etching methods. a) Unetched substrate. b) Chemical, wet isotropic etching. c) Physical, dry anisotropic etching.

In device microfabrication, etching refers to a process that will selectively remove material from the substrate, thereby producing the resulting pattern on the substrate.

Etching can be divided into wet (see Fig. 2.5b) and dry (see Fig. 2.5c) etching. To characterize etching, several factors such as etch rate, selectivity, and isotropy are used to characterize etching. These are the factors that distinguish wet and dry etching.

Selectivity describes how fast one material is etched compared to another. An etch-resistant mask should be etched slower than the material that is being etched. In other words, selectivity is defined as the ratio of the etch rate of the etched material and the etch rate of the masking material. The directionality of etching divides the etching process into isotropic and anisotropic.

In most cases, chemical wet etching is isotropic—there is the removal of the material in all directions, which causes a slightly different transfer of the motive from the mask to the substrate. Dry etching on the other hand is anisotropic, where the removal of the material is achieved by reactive ions.

2.3.1 Reactive ion etching

RIE – reactive ion etching is the type of dry directional etching which uses chemically reactive plasma to remove material deposited on the substrate. It is the combination of chemical and physical reactions that remove material from a surface. It is a strongly anisotropic etch that is achieved by energetic, highly directional ion bombardment of the sample during chemical plasma etching. The plasma is generated under low pressure by an electromagnetic field. High-energy ions from the plasma are accelerated towards the negatively biased substrate and react with it.

The reactive ion etching, in order to transfer the pattern from the resist to the SiO_2 layer, was performed using an Oxford Instruments Plasma Technology PlasmaPro 100 industrial reactor. The etching was performed using a combination of C_4F_8 and O_2 . The etching process involved several steps, specifically oxygen stabilization, breakthrough, gas stabilization, the etching step itself, and finally the pumpout. The parameters of this etching process are shown in the Tab. 2.1.

Table 2.1: Used parameters of RIE process.

	ICP (W)	HF (W)	Pressure (mTorr)	SF_6 (sccm)	C_4F_8 (sccm)	O_2 (sccm)	Time (s)	Temp (°C)
Oxygen stab	0	0	40	0	0	50	10	5
Breakthrough	1500	50	40	0	0	50	12	5
Gas stab	0	0	10	0	40	8	15	5
Etching	2500	85	10	0	40	5	15	5
Pumpout	0	0	0	0	0	0	30	5

2.3.2 Deep reactive ion etching

The following process technology is a modified version of RIE, DRIE—deep reactive ion etching which is used to etch deep structures. Through this process the silicon substrate can be etched through. It is highly anisotropic. There are two types of this technology—cryo, where the structure is etched at very low temperatures, and the Bosch process. The Bosch process repeatedly alternates between two modes—the standard near-isotropic ion etch (see Fig. 2.6c), and the deposition of a passivation layer (see Fig. 2.6b) that protects against further etching. The directional ions attack the passivation layer during further etching at the bottom, but not so much at the sides. By alternating these two steps, the scalloping characteristic of this process is formed on the walls of the etched substrate.

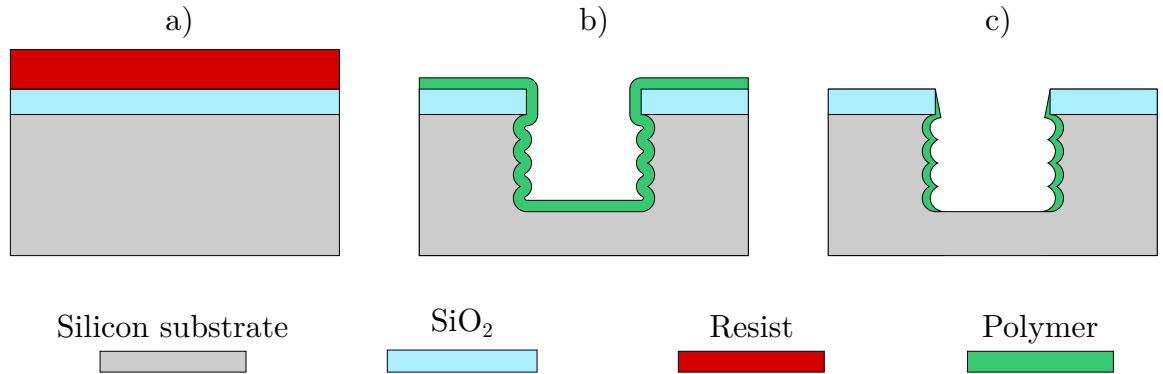


Figure 2.6: Deep reactive ion etching. a) Unetched substrate. b) Passivation step. c) Etching step.

Deep reactive ion etching to transfer the pattern to the silicon substrate and also to deepen the pattern was performed on an Oxford Instruments Plasma Technology PlasmaPro 100 industrial reactor. The etching was performed using a combination of SF₆ and C₄F₈, with SF₆ used for etching and C₄F₈ for deposition. The process consisted of initial gas stabilization and strike steps to initiate the discharge in the plasma. Subsequently, in a loop of 200 cycles, the deposition, two breakthroughs, and then etching steps were performed in this order. At the end of the process, pumpout took place. The most important thing about this process is the correct ratio of deposition to etching so that the etching is directional in depth. For example, there should not be a conical etch, which would be caused by too much passivation of the walls, meaning that the passivation step is too long compared to the etching. The important thing for the smoothest walls, and therefore the smallest scallop, is that the steps are very short and alternate very quickly. The resulting etching parameters can be found in the Tab. 2.2.

Table 2.2: Used parameters of DRIE process.

	ICP (W)	HF (W)	Pressure (mTorr)	SF ₆ (sccm)	C ₄ F ₈ (sccm)	O ₂ (sccm)	Time (s)	Temp (°C)
Gas stab	0	0	10	10	10	50	15	0
Strike	1500	100	30	10	10	50	5	0
Deposition	1750	0	40	10	200	0	1	0
Breakthrough A	2000	0	25	200	10	0	0.5	0
Breakthrough B	2000	20	20	200	10	0	0.6	0
Etching	2000	0	20	200	10	0	0.3	0
Pumpout	0	0	0	0	0	0	30	0

2.3.3 Black silicon etching

The black silicon etching, also known as b-Si etching, is a type of cryo-process deep-reactive ion etching. The textured silicon surface appears to the human eye as a black surface, hence the name black silicon. It is a micro-texturing of the silicon using a fabrication process involving O₂/SF₆ reactive ion etching at cryogenic temperatures. Thanks to this etching process, it is possible to obtain structures with a very high aspect ratio.

The search for the process window where black silicon forms on the substrate was carried out by varying several plasma process parameters such as the O₂/SF₆ gas flow rate ratio, the temperature, the bias voltage, and the etching time. By observing these parameters, the process window in which black silicon formation occurs was found. Also the changes in the morphology of the resulting b-Si at different parameters were observed.

The DRIE process results in anisotropic etching of the silicon using inductively coupled plasma (ICP) of sulphur hexafluoride (SF₆) and oxygen (O₂). It works on the principle of the wall passivation mechanism. SF₆ gases produce fluorinated radicals F* for chemical etching of silicon, leading to volatile SiF₄, which can be described as



At the same time, fluorinated radicals react with silicon and form SiF_x sites on its surface, which then react with O* oxygen radicals to form lateral passivation layers SiO_yF_x. The passivation layers are very important in the formation of black silicon.



The presence of oxygen determines the formation of the passivation layer SiO_yF_x

which is the crucial ingredient in the creation of black silicon. This passivation layer forms only at cryogenic temperatures.[26]

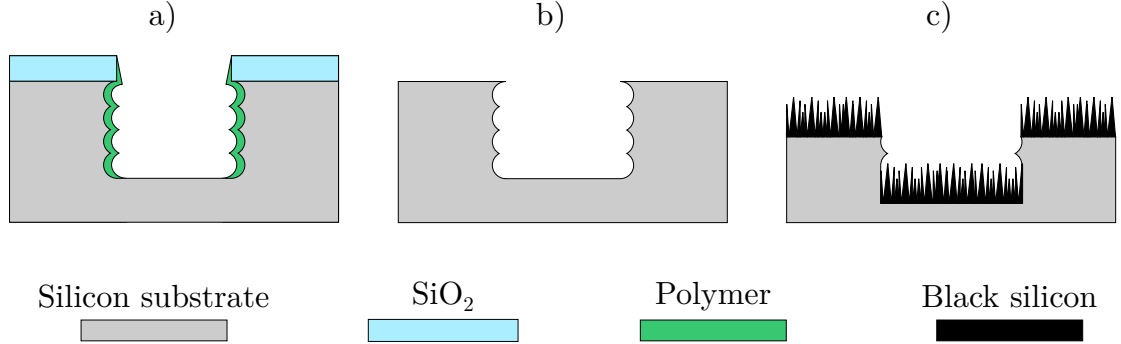


Figure 2.7: Black silicon etching. a) Unetched substrate. b) Oxide removal using BOE. c) Black silicon.

The surface treatment of the samples on top of the already formed pillars using the Bosch process was carried out on the same Oxford Instruments Plasma Technology PlasmaPro 100 industrial reactor.

The etching was supported by the presence of SF_6 whose flow rate was fixed at 200 sccm and O_2 whose flow rate was varied from 20 sccm to 50 sccm. The experiments were carried out at temperatures between -100 and -115 °C for 5–20 minutes. The ICP (Inductively Coupled Plasma) power was fixed at 1,000 W. The pressure value varied from 20 mTorr to 11.5 mTorr. The bias voltage was influenced by varying the HF (high frequency) source power from 25 W to 3 W.

The specific measurement parameters for each sample are shown in the Tab. 2.3, where the samples on which black silicon was successfully formed are highlighted.

Table 2.3: Variable investigated parameters of the cryogenic DRIE process in the formation of black silicon.

	1	2	3	4	5	6	7	8
Ratio of O_2/SF_6	0.1	0.15	0.25	0.15	0.15	0.15	0.25	0.2
Temperature (°C)	-115	-115	-115	-115	-100	-115	-115	-115
Etching time (min)	10	10	10	20	10	10	10	10
HF power (W)	25	25	25	25	25	5	3	3

The sample 6 was prepared in two stages. The ICP power was fixed at 1,000 W, the flow rate SF_6 at a fixed value of 200 sccm. In the first phase, the O_2 flow rate was set at 30 sccm, which gives an O_2/SF_6 ratio = 0.15, and etching was performed at -115 °C for 10 minutes at an HF value of 5 W. This recipe did not result in the formation of black silicon, so another process was run on the same sample with adjusted O_2/SF_6 =

0.25, the O_2 flow rate was increased to 50 sccm and the sample was etched at an HF value of 3 W for 5 minutes. Through this process, black silicon was formed. The sample number 6 can be seen in Fig. 2.8a) from the top-view and in Fig. 2.8b) at an angle of 50° .

Thus, the previous experiment above led to the finding that to form black silicon, the oxygen flow rate needs to be increased. Thus, the sample 7 was etched with fixed parameters ICP–1,000 W, SF_6 - 20 sccm. HF was set to 3 W and the oxygen flow rate according to the previous experiment was set to 50 sccm, therefore the O_2/SF_6 ratio is 0.25. The etching at these parameters was carried out for 10 min and led to the formation of black silicon – its topography from the top is shown in Fig. 2.8c) and at an angle of 50° in 2.8d).

The experiment was performed on the sample 8 with the same parameters as before i.e. ICP–1,000 W, SF_6 –20 sccm, and HF was set to 3 W. Only the oxygen flow rate was changed to a lower value of 40 sccm. This experiment was done to find the process window at which the O_2/SF_6 ratio of black silicon is still formed and at which the oxygen flow rate is too low to form black silicon. The sample 8 can be seen in Fig. 2.8a) from the top-view and in Fig. 2.8b) at an angle of 50° .

It was found that the minimum ratio for black silicon formation is $O_2/SF_6 = 0.2$. If this ratio is lower, no further black silicon formation occurs, even if the etching time is increased.

Table 2.4: Resulting parameters of the black silicon etching process.

	ICP (W)	HF (W)	Pressure (mTorr)	SF_6 (sccm)	C_4F_8 (sccm)	O_2 (sccm)	Time (s)	Temp ($^\circ C$)
Cooldown	0	0	0	0	0	0	180	-115
Gas stab	0	0	11.5	196	105	22	10	-115
Strike	1750	50	30	5	105	50	5	-115
Step	1000	25	11.5	200	0	50	10	-115
Etching	1000	3	11.5	200	0	50	600	-115
Pumpout	0	0	0	0	0	0	30	-115

The final selected O_2/SF_6 ratio for the samples in this work is 0.25. The etching process included several extra steps for proper progression, namely the cooldown, the gas stabilization, the strike for proper initiation of the discharge in the plasma, the extra step for plasma initiation and stabilization, the etching step itself, and, finally, the pumpout. The parameters of these steps are given in the Tab. 2.4.

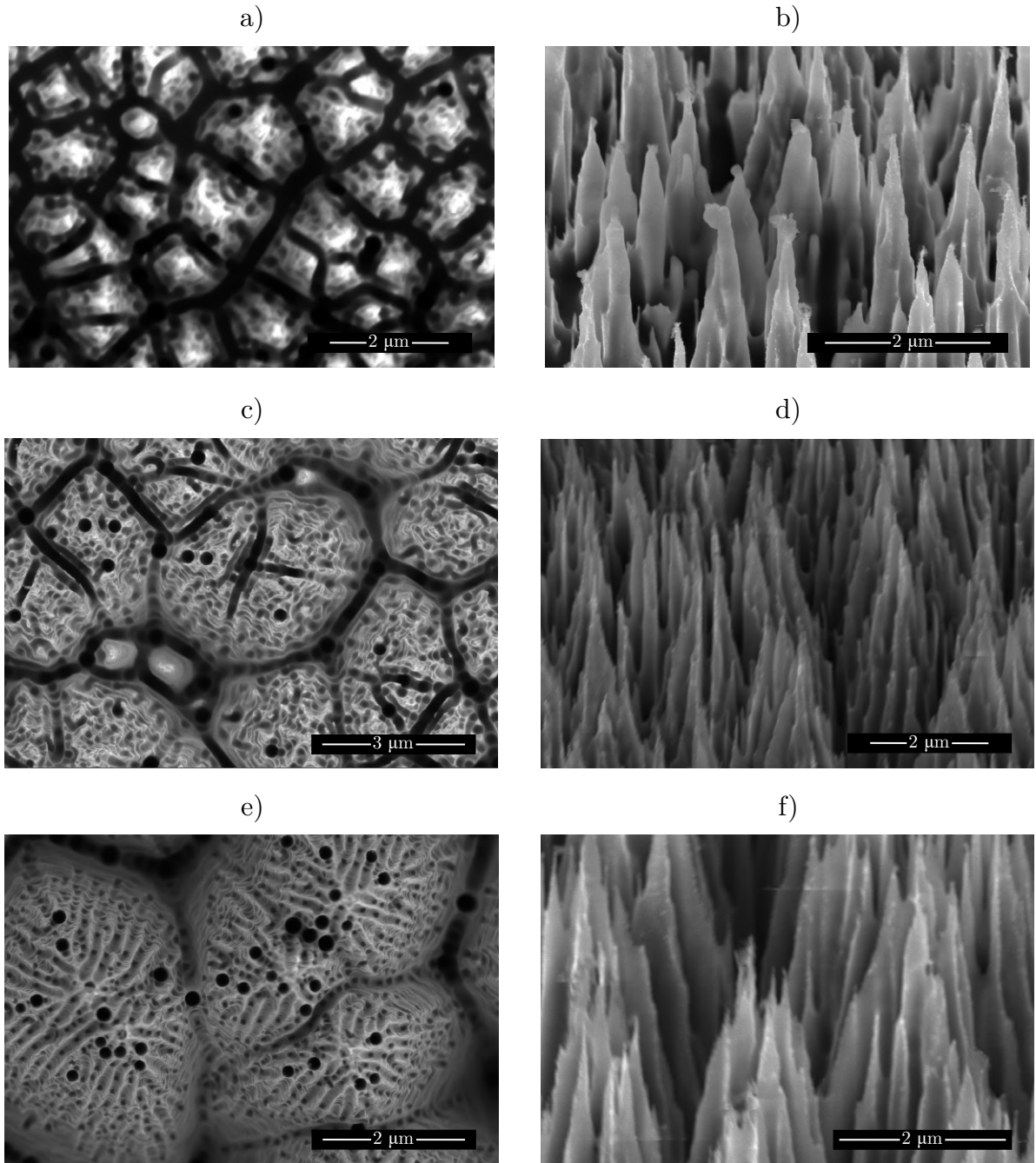


Figure 2.8: The top-view and the 50° tilted view of the SEM images of black silicon formed on samples 6, 7, 8. a) The top view of sample 6. b) the 50° tilted view of sample 6. c) The top view of sample 7. d) The 50° tilted view of sample 7. e) The top view of sample 8. f) The 50° tilted view of sample 8.

3. MEASUREMENTS AND RESULTS

3.1 Sample topography

Investigating the topography of the sample using various advanced techniques is key in micro and nanofabrication since it cannot be observed with the human eye. After each technological step in sample fabrication, it was necessary to observe the topography of the sample using a scanning electron microscope or a confocal microscope (see Fig. 3.1). The chemical composition of the sample surface was determined by X-ray photoelectron spectroscopy.

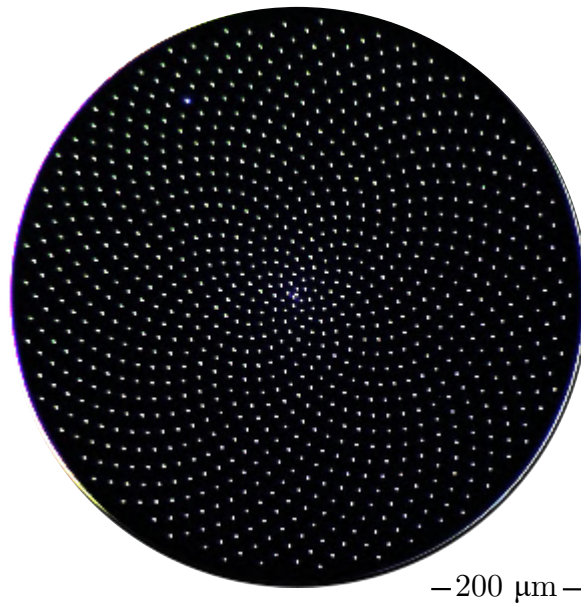


Figure 3.1: Structure containing 5,000 emitters captured on a confocal microscope.

3.1.1 Scanning electron microscopy

The basic principle of the scanning electron microscope is imaging a sample by scanning the surface of the sample using accelerated electrons focused into an electron beam. These accelerated electrons interact with the atoms of the sample, thus providing information about the topography of the sample. When interacting with the sample at different interaction volumes, different types of electrons are emitted and can be measured, such as secondary electrons, backscattered electrons, and Auger electrons. The electron beam scans the surface of the sample and the intensity of the detected signal is measured to produce an image.

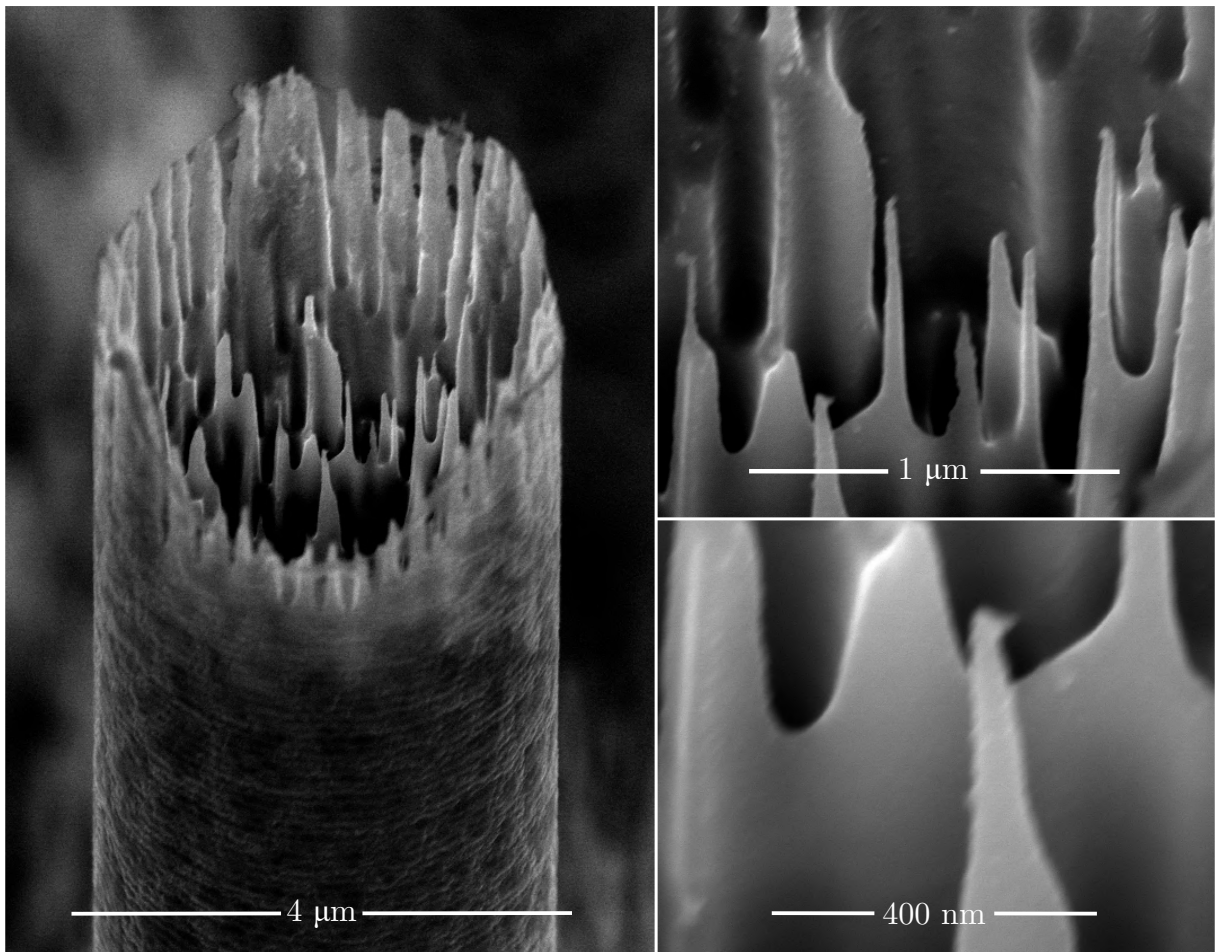


Figure 3.2: The detail of the emitter and black silicon on the top of the emitter. Photos taken at accelerating voltage 5 kV and current 50 pA.

All photos in this chapter are taken in the secondary electron detection mode. The method is based on the principle of measuring the number of incident secondary electrons on the detector, i.e. the signal intensity. The secondary electrons are collected by a positively biased collector grid which is placed on one side of the sample; their work function is low. A scintillator is placed behind the collector grid on which the

electrons are accelerated. The scintillator generates light quanta and these are recorded by a photomultiplier. The signal intensity of the secondary electrons depends on the tilt angle of the surface element and there is increased emission at the edges and small particles. Incomplete electron collection causes shadow contrast. This allows an image of the sample topography to be constructed.[27]

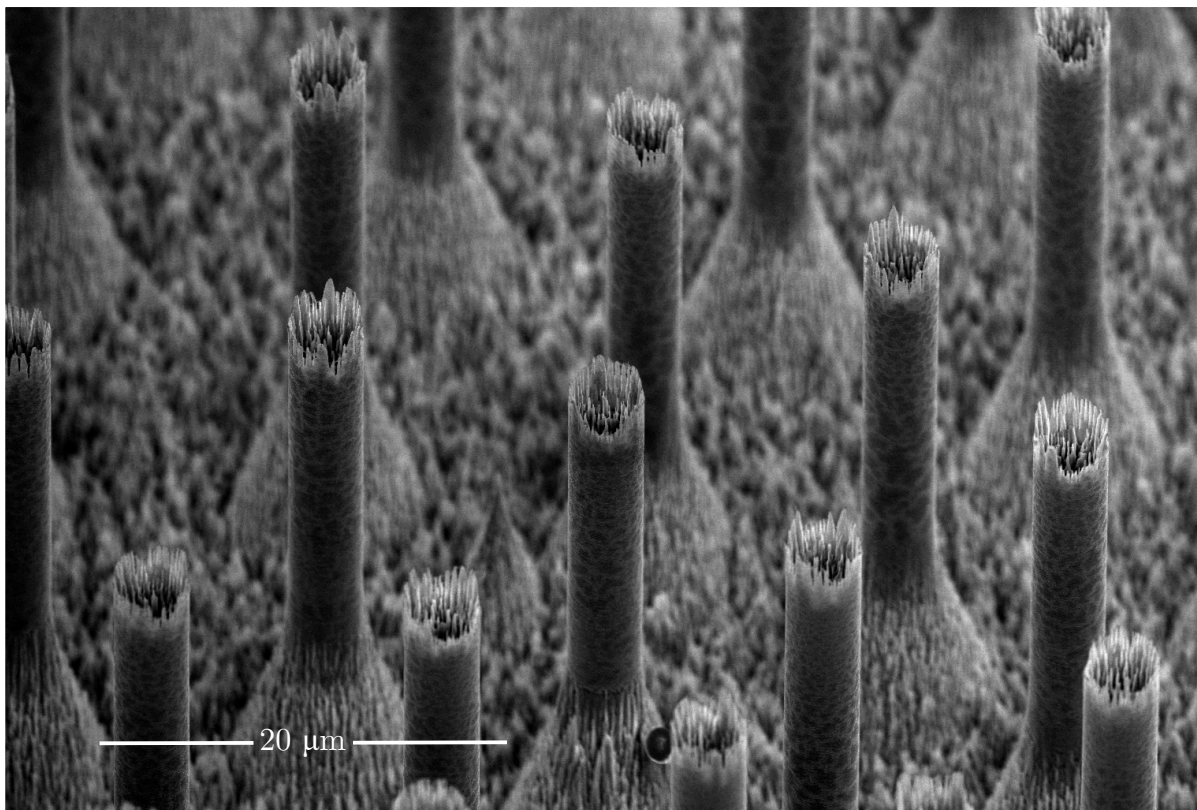


Figure 3.3: Multiple emitters in FEA. Photos taken at accelerating voltage 5 kV and current 50 pA.

The photos (see Fig. 3.2 and Fig. 3.3) in this chapter were taken using Verios 460L, a High-resolution Scanning Electron Microscope from Thermo Fisher Scientific.

3.1.2 X-ray photoelectron spectroscopy

X-ray photoelectron spectroscopy is one of the most widely used material analysis techniques based on the principle of the photoelectric effect. It is a surface-sensitive analytical technique that involves bombarding a surface with x-rays, this causes the emission of electrons and their kinetic energy is subsequently measured. The characteristic of this method is its surface sensitivity and its ability to reveal chemical state information from elements in the sample.

Factors such as surface wettability, adhesion, corrosion, and others are determined by surface properties and surface contamination, and therefore, it is important to

examine and understand surfaces. In this particular case, surface contamination can very significantly (even in the order of electron volts) affect the work function, one of the basic parameters that determine the emission properties.

The sample is irradiated with x-rays with energies lower than 6 keV, while the kinetic energy of the emitted electrons is measured. The x-ray energy is completely transformed in the form of the emitted electron, it is equal to the binding energy (BE) of the electron, plus the kinetic energy (KE) of the electron that is emitted, plus the spectrometer work function ϕ_{spec} . This is shown in the schematic Fig. 3.4 and described by the equation

$$h\nu = \text{BE} + \text{KE} + \phi_{\text{spec}}. \quad (3.1)$$

It is important to remember that the photoelectron binding energy is related to the sample Fermi level, not the vacuum level, therefore it is necessary to include the spectrometer work function.

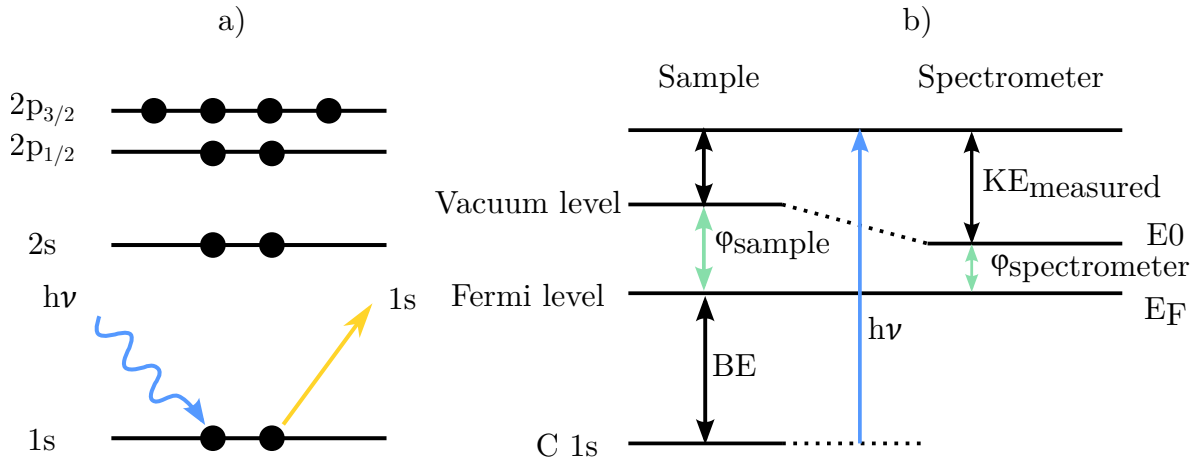


Figure 3.4: a) X-ray bombardment of a surface and the subsequent emission of a photoelectron. b) Energy level diagram illustrating the basic XPS equation. Adapted from [28].

XPS is a surface-sensitive technique even though X-rays can penetrate deep into the sample on the order of a few μm . This is because electrons that are generated deeper in the material undergo many inelastic collisions, thus losing their energy and not exiting the sample. Electrons that are generated closer to the surface undergo one or two inelastic collisions, and therefore have lower kinetic energy. These electrons contribute to the background signal near the large photoelectrons.[28]

Fig. 3.5 shows the resulting measured spectrum of the auto emission structure sample. This spectrum was processed in CasaXPS, a program used to analyze XPS data, and then plotted in Python. Calibration was the first thing that had to be done as surface charging can affect the spectrum. Charge accumulation can create dipole layers that shift the measured binding energies. This calibration was performed according to

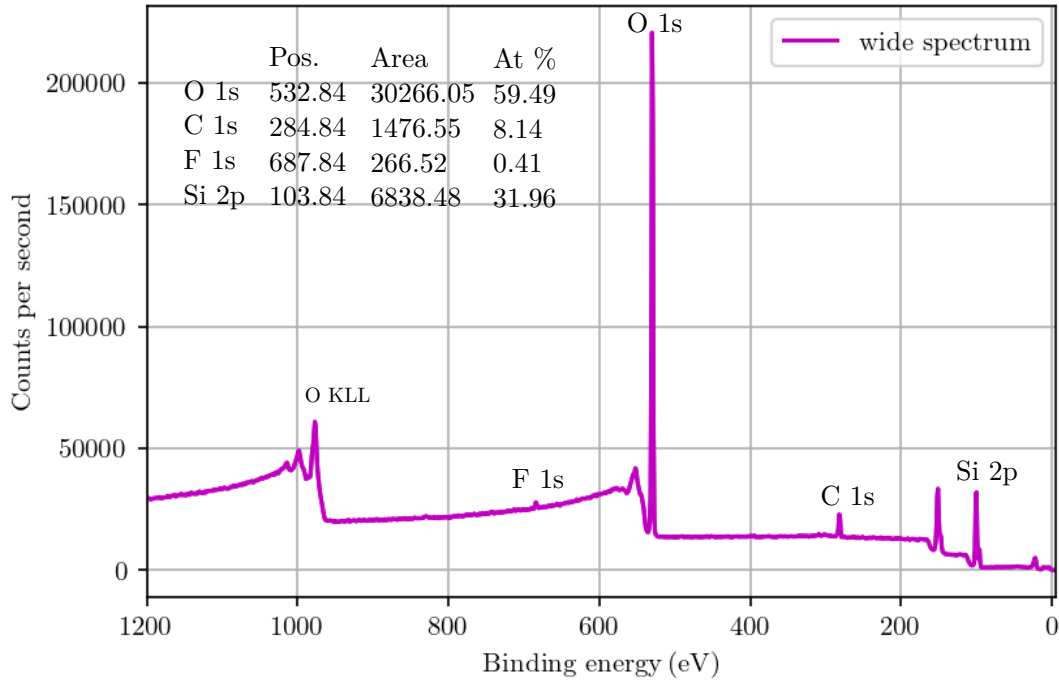


Figure 3.5: Wide XPS spectrum.

the carbon C 1s peak since almost all surfaces have some carbon contamination after exposure to the atmosphere. The C 1s carbon peak was shifted to a value of 284.6 eV and with it the entire spectrum.

Subsequently, quantification was performed, finding the percentage of elements on the sample surface. As mentioned earlier, the C 1s peak is explained by surface contamination of the sample after exposure to the atmosphere. The highest abundance of 59.49 % is O 1s on the sample. This is also due to the exposure to the atmosphere and it may also be influenced by the last step of surface treatment of the sample, the oxygen plasma cleaning. It may also be because there is a relatively large area of SiO₂ around the emission structure on the chip. This also explains the additional Si 2p component of 31.96 % which is not surprising given that it is a silicon substrate. The peak F 1s, which has the smallest representation of 0.41 %, can be explained by the fact that fluor compounds were used in all etching steps. Thus, the XPS measurement result did not reveal anything surprising, by all means, it may be highly influenced by the surrounding of the structure which is covered by the SiO₂ layer.

The peak O KLL represents the energy of the electrons ejected from the atoms due to the filling of the O 1s state (K shell) by an electron from the L shell coupled with the ejection of an electron from the L shell.

3.2 Field emission microscope

Measurements of the emission behavior of the fabricated auto emission structures with ultra-sharp tips were performed on an electron source set-up inside an ultrahigh vacuum chamber with a pressure as low as 10^{-7} Pa. The entire vacuum electron source set-up had a milled stainless steel frame.

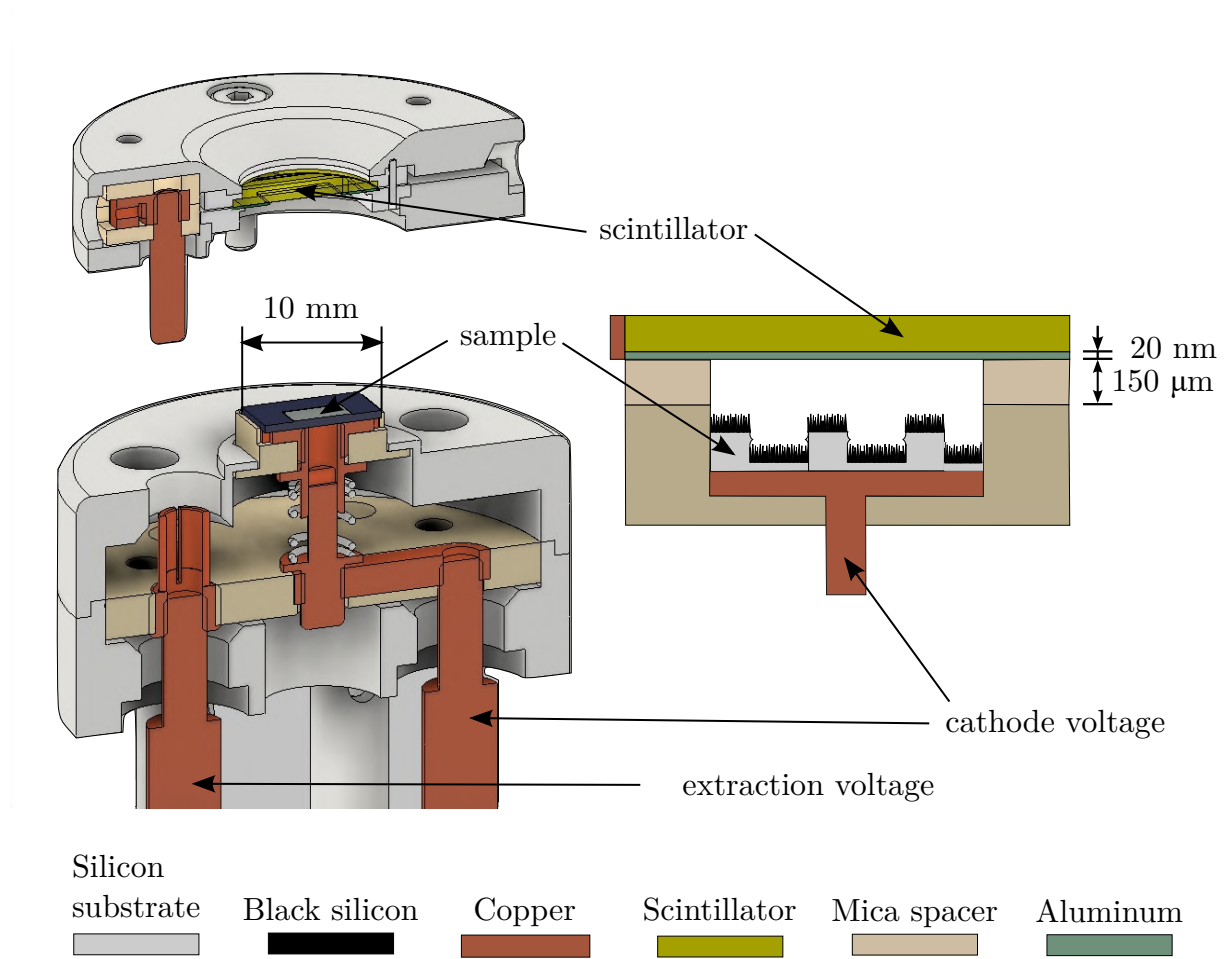


Figure 3.6: The field emission microscope set-up.

The set-up described below is shown in the Fig. 3.6. The sample itself is placed on a copper pad to which a spring is attached. The spring is used to keep the sample as tightly attached to the spacer as possible and to prevent any residual space between the sample and the spacer. The spring can be screwed in and the pressure of the sample can be controlled so that it does not move during handling. Around the sample, there is an indentation of the insulating material so that there is no sideways movement. The set-up is therefore designed for a maximum sample size of (8×8) mm. A cathode voltage is applied to the copper pad under the sample and goes to the sample. For better electrical contact between the copper pad and the sample, the sample is held in place with silver conductive paste. A mica spacer, 150 μm thick, is placed on the

sample with a (5×5) mm cutout so that only the emission structures are exposed to the scintillator. A scintillator is attached to the insulating layer of the mica spacer on which a conductive, 20 nm thick layer of aluminum is deposited from the bottom layer. An extraction voltage is applied to the scintillator, so the conductive layer serves to conduct the emission current which can be measured. A conductive wire is attached to the scintillator and connected to a positioning pin. The positioning pin connects the top of the set-up where the mica spacer and the scintillator are located at the bottom of the set-up where the sample is located. The pin is inserted into the extraction voltage supply.

3.2.1 Field emission imaging

For field emission imaging, i.e. the display of the emission pattern on the screen, a scintillation crystal was used. The scintillation crystal is made of powder phosphor and is used to detect the electron signal.

A scintillator is an absorbing material that has the ability to convert the energy of ionizing radiation into the energy of photons and therefore the light. The charged particles interact with the scintillator electrons through Coulomb interactions, this leads to excitation or ionization of the scintillator atoms.

In this case, a scintillator crystal is used to convert the energy of the emitted electrons from the auto emission structure. These emitted electrons interact with the scintillator and their energy is converted to the energy of visible light photons. Thus, thanks to this mechanism, we are able to observe the emission behavior with the naked eye.[\[29\]](#)

In this measurement, a cerium-doped YAG:Ce scintillator crystal was used. A camera was placed behind the scintillator to capture images.

The first emission pattern (it can be seen in Fig. [3.7a](#)) started to appear at approximately 2300 V when one point on the scintillator illuminated. This corresponded to a current of approximately 0.13 μA . The emission pattern in Fig. [3.7b](#)) corresponded to a voltage of approximately 3200 V and 7.3 μA . When exceeding 3600 V, the individual emission points could no longer be distinguished and the exact number determined, which corresponds to Fig. [3.7c](#)) and a current of 15.8 μA . Pattern [3.7d](#)) was taken at 3830 V and a current of 50 μA . Pattern [3.7e](#)) was taken at 3900 V and a current of 62 μA . Pattern which can be seen in the Fig. [3.7f](#)) was taken at 4000 V and a current of 68 μA . Pattern [3.7g](#)) was taken at 4300 V and a current of 94 μA . And then it started to burn out even though the current kept increasing [3.7h](#)) 4250 V and 0.3 mA and at the same voltage there was a rapid drop in current [3.7h](#)) to 4 μA .

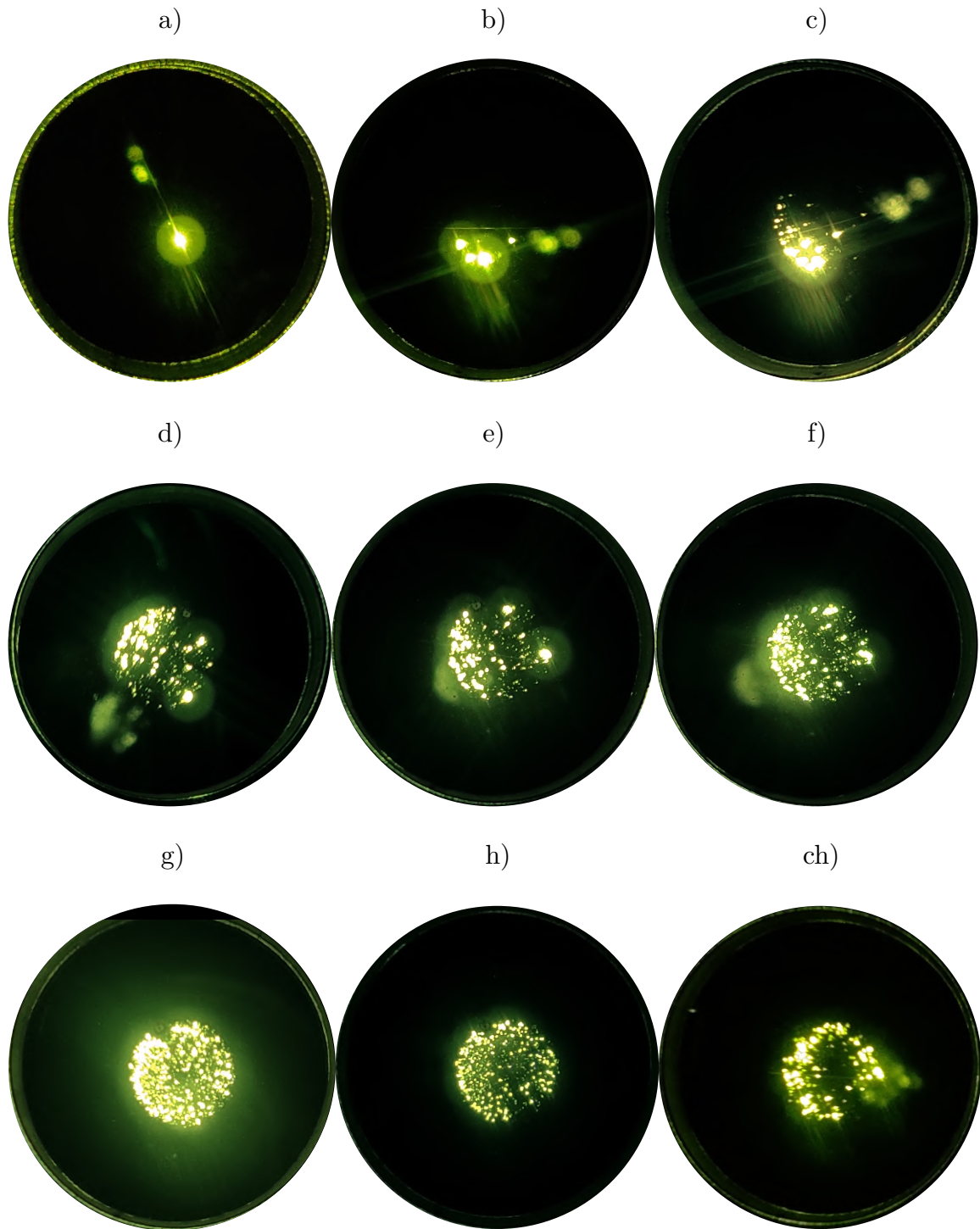


Figure 3.7: Emission patterns for gradually increasing voltage.

3.3 Electrical properties

3.3.1 Ultraviolet photoelectron spectroscopy

UPS or Ultraviolet photoelectron spectroscopy is a technique that can be performed on XPS systems that are equipped with an ultraviolet source, most commonly a He-I source, which has an energy $h\nu$ of 21.22 eV. In principle, this technique is the same as XPS, however, the sample is irradiated with a UV source instead of an x-ray source. The ultraviolet source has much lower energy than the x-ray source and, for this reason, cannot eject electrons from the inner shells. It can only eject valence electrons at higher levels which have low binding energies. This technique is very sensitive to surface contamination because only the surface layer of about 2–3 nm thickness is analyzed due to the low-energy UV source.

The UPS spectra are essentially density of states diagrams with a focus on the energy levels just below the Fermi level. The work function can be determined from this spectrum whose energy value lies between the Fermi level and the vacuum level. Also, using this spectroscopic technique, it is possible to detect ionization energy, the energy between the vacuum level and the first valence level in a semiconductor.[28]

Measurements of the UPS spectrum were performed on an X-ray Photoelectron Spectroscopy Axis Supra (KRATOS-XPS). The spectrum of a silicon chip covered with black silicon was measured. UPS measurements were not performed on the final auto emission structures due to the fact that the area of the chip covered by black silicon was very small and, due to this, the resulting work function was distorted by the background which is covered by a layer of SiO_2 .

The spectrum in Fig. 3.8 shows a clear Fermi edge at 1,295 eV and occupied states just below the Fermi edge between approximately 6 and 11 eV. When the energy approaches approximately 16 eV, the intensity drops very rapidly. Electrons with higher binding energy are not probed because the energy of the ultraviolet source is not able to eject these electrons. This part of the energy spectrum is called the secondary electron cutoff (E_{cutoff}). The work function can be determined using E_{cutoff} and E_{Fermi} from the equation

$$\varphi = h\nu - (E_{\text{cutoff}} - E_{\text{Fermi}}). \quad (3.2)$$

The spectrum of black silicon was measured at two different positions on the sample with black silicon. Due to the high sensitivity to surface contamination, the sample was cleaned in the device and the surface layer of impurities was sputtered with argon ions. The results found by E_{cutoff} and E_{Fermi} and the work function calculated by using them are shown in the tables.

In Tab. 3.1, two positions (labeled 1 and 2) on the uncleaned sample were measured and two E_{cutoff} values were found for each position (distinguished as 1.1 and 1.2 and, similarly, 2.1 and 2.2); these values were then averaged. The resulting work function of the uncleaned sample is $\varphi_{b-Si} = 5.783$ eV.

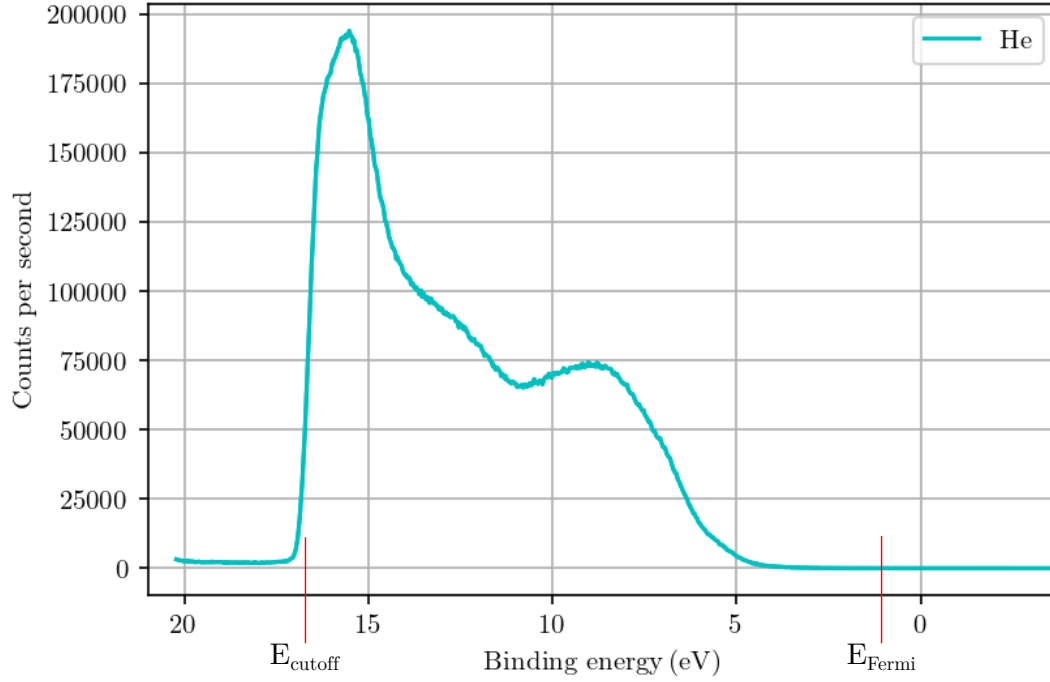


Figure 3.8: The UPS spectrum for Black silicon.

In Tab. 3.2, two positions (labeled 3 and 4) on the argon cleaned sample were measured and two E_{cutoff} values were found for each position (distinguished as 3.1 and 3.2 and, similarly, 4.1 and 4.2); these values were then averaged. The resulting work function of the sample cleaned with argon is $\varphi_{b-Si-cleaned} = 5.033 \text{ eV}$.

Table 3.1: UPS results of black silicon.

	E_{cutoff}	E_{Fermi}	φ
1.1	16.595	1.295	5.920
1.2	16.620	1.295	5.895
		average	5.908
2.1	16.545	1.045	5.720
2.2	16.670	1.045	5.595
		average	5.658

3.3.2 I-V characteristics

The I-V characteristic is essential to characterize the emission behavior. This characteristic was measured using the set-up described in section 3.2. The emission structure was placed in an ultravacuum chamber and electrically connected via a coaxial cable to

Table 3.2: UPS results of black silicon on argon cleaned sample.

	E_{cutoff}	E_{Fermi}	φ
3.1	17.295	1.120	5.045
3.2	17.345	1.120	4.995
		average	5.020
4.1	17.520	1.370	5.070
4.2	17.570	1.370	5.020
		average	5.045

a custom power supply from Delong Instruments, and to a Keithley 485 picoammeter. The measured I-V characteristic is shown in the Fig. 3.9.

The emission behavior shows a very high onset field, with the onset of stable emission with an emission current of approximately 130 nA occurring at a voltage of approximately 2.3 kV. At lower voltages, the emission current was very small and very unstable. When the voltage exceeded 2.7 kV, the emission current began in the order of units of μA . With further voltage increases, there was a rapid exponential increase in the current.

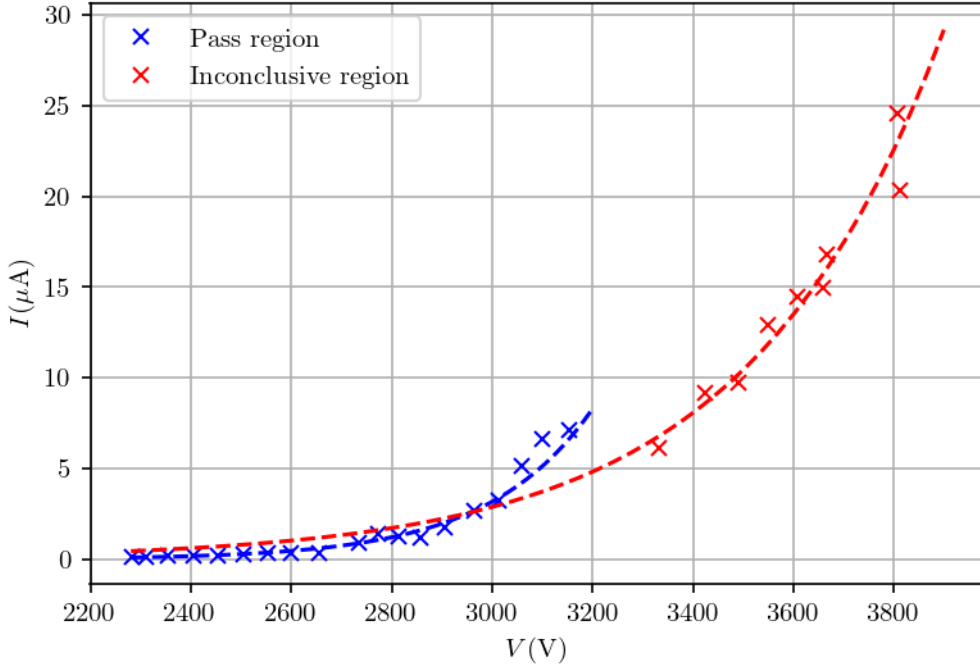


Figure 3.9: The I-V characteristics.

When measuring the I-V characteristic, the current increases as the voltage increases. Since the measurement is not done in an absolute vacuum, there is a certain presence of gases gathering on the top of the surface, which means that, at some point

there must be, for example, a change in the chemical composition of the sample surface. Alternatively, some emitters on the surface may be destroyed, causing a change in parameters.

For this reason, it is necessary to verify the quality and validity of the experimentally measured I-V characteristic. For this purpose, the Field emission orthodoxy test is used, a qualitative test that checks the reasonableness of the information that is obtained from these plots.

The Murphy-Good (M-G) plot is used to analyze the emission data (see Fig. 3.10). When the system is orthodox, then the M-G plot is a nearly straight line from which the emission parameters can be determined. Orthodox means that it can be said, using a suitable approximation, that the tunneling is through a Schottky-Nordheim (plane-rounded) barrier and hence there is no voltage dependence in the emission region or in the local work function. [30]

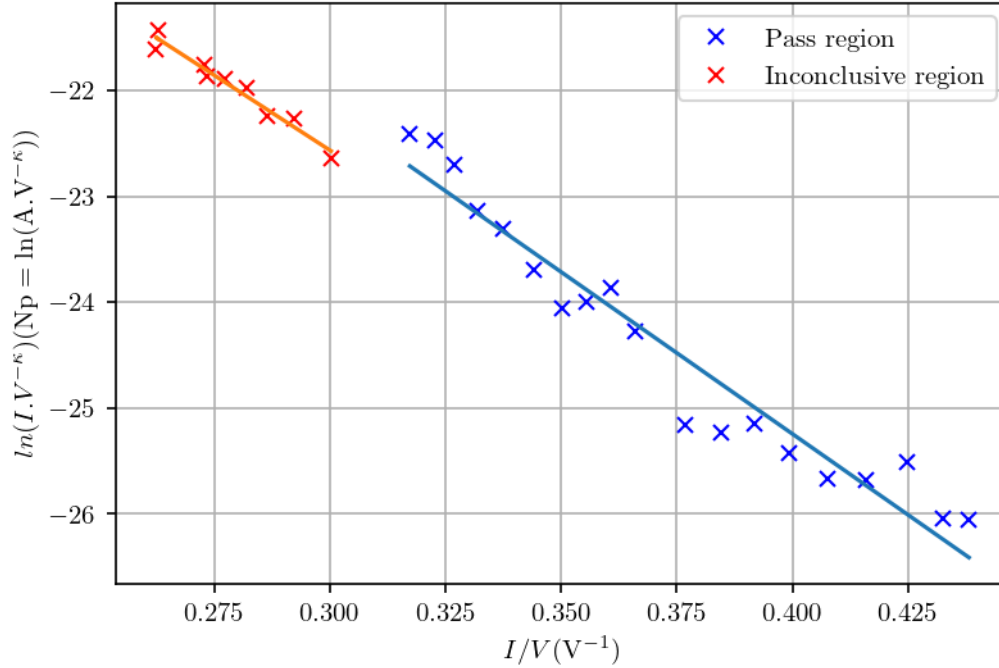


Figure 3.10: The Murphy-Good analysis plot.

The I-V characteristic was divided into regions. A Pass region means operating in the low-voltage regime, where the number of ionized gas molecules still does not affect the emission process. It means that we are operating in the acceptable voltage range regime which is related to the allowed scaled field range of the corresponding work function. If we exceed this acceptable voltage range, we are operating in an Inconclusive region. [31]

The first is the Pass region, which in this case lies between approximately 2500 V and 3100 V. After crossing the higher boundary of this region, it appears that all

Table 3.3: The field electron emission orthodoxy test and analysis results.

Line	Test result	A_f^{SN}	ϵ	γ
red	Pass	5.93	407	368.14
blue	Inconclusive	0.37	3.52	427.91

emitters have started to contribute to the emission current, i.e. they have started to emit. We refer to this region as Inconclusive. Measuring emissions in this region is also safe, but some caution must be exercised. Once the Inconclusive region is crossed, the surface of the sample is destroyed, the individual emitters are damaged, and it is no longer possible to clearly identify the origin of the emission. In this case, it was safe to measure up to a current value of 24 μA .

In the safe interval, when the samples have passed the orthodox test, the parameters characterizing the emitters can be obtained from the Murphy-Good plot. Specifically, the formal emission area A_f^{SN} for the S-N (Schottky–Nordheim) barrier, it can be defined as the area that is extracted from the plots of the experimental data analysis and that provides the desired information about the region where the emitted electrons left the tip surface. Furthermore, the characteristic voltage conversion length (VLC) parameter ϵ , which is not a physical length, refers to the needed "turn on" voltage; at low VCL values, the emitter "turns on" at a low voltage. And last, the field enhancement factor γ . The mentioned results are shown in the Tab. 3.3.

3.3.3 Total emission current stability

The total emission current stability was measured using an RBD 9103 picoammeter which records the current overtime on a connected computer using the RBD Actuel software with an A/D converter in place. The sampling rate is 40 reads per second, i.e. it measures the current every 25 ms. The current stability was measured for 3 different voltages for 40,000 ms, the obtained data is plotted in the Fig. 3.11.

The calculation of the stability of the current over time for a voltage of 3024 V showed that when the data is fitted with a normal distribution (Gaussian curve), 95 % of the values of the measured current are in the range of 82 nA. This is a very small interval and, therefore, we can declare the current as stable with a value of 139 ± 41 nA. For a voltage of 3132 V, it came out that 95 % of all measured current values were in the range of 39 nA. So, the current is very stable at 152 ± 20 nA. The current stability for the highest measured voltage of 3435 V came out as the most fluctuating, but still very accurate, as 95 % of the measured current values are in the range of 134 nA. The current at this voltage can therefore be determined as 425 ± 67 nA.

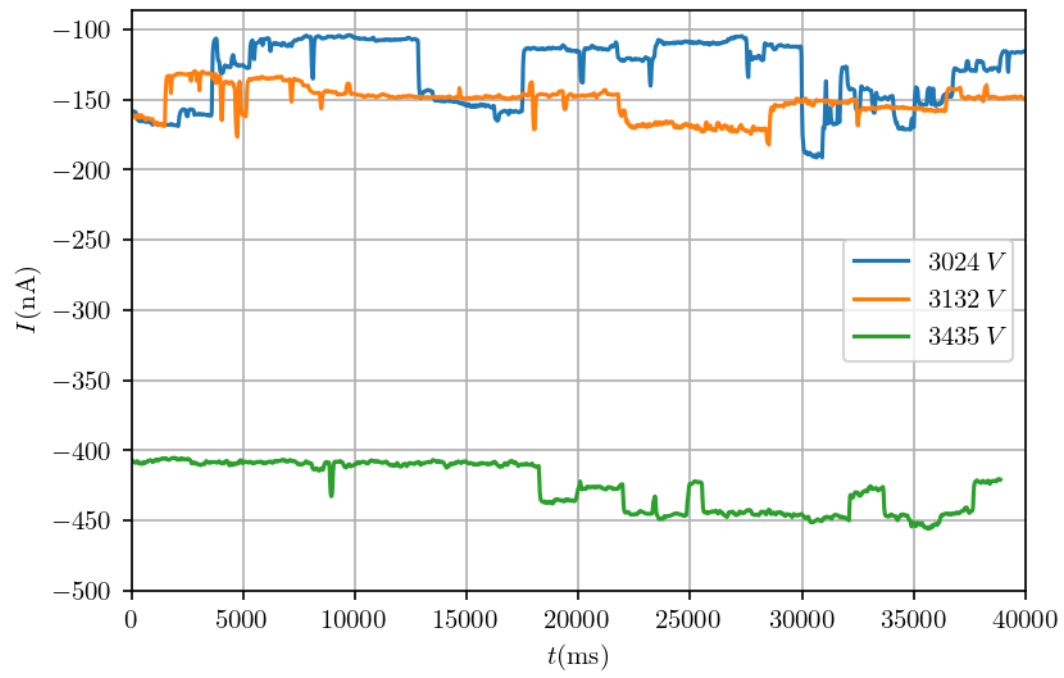


Figure 3.11: The current stability.

CONCLUSIONS

In this thesis, structures of high aspect ratio field emitters were fabricated with an arrangement resembling that of sunflower seeds according to a natural phenomenon called phyllotaxis. Pillars were successfully created with a diameter of 3.5 μm and a height of 25.5 μm using electron and laser lithography. Subsequent reactive ion etching and deep silicon etching using the Bosch process made it possible to achieve this height-to-diameter ratio. On top of the micropillars, ultra-sharp tips with a radius of less than 50 nm were formed using black silicon etching in a cryo DRIE process.

The topography of the sample was examined by the scanning electron microscopy. X-ray photoelectron spectroscopy was used to determine the chemical composition of the sample surface. It revealed that silicon and oxygen have the highest percentages of approximately 32 % and 60 %, respectively. The oxygen on the sample could represent contamination due to the final cleaning of the samples with oxygen plasma which could increase the work function. However, it could also be a signal caused by the surroundings of the emission structures which are covered by a layer of SiO_2 .

Using Ultraviolet photoelectron spectroscopy, the work function on the sample covered with black silicon was investigated. The work function was first determined as $\varphi_{b-Si} = 5.783 \text{ eV}$ for the sample that was not cleaned of surface contamination. After subsequent cleaning of the sample with argon ions, its work function was determined to be $\varphi_{b-Si-cleaned} = 5.033 \text{ eV}$. This means that impurities on the surface could increase the work function of the sample.

The set-up of the field emission microscope was modified so that the fabricated sample could serve as a cathode and, this way, its emission properties could be determined. An insulating layer of mica spacer was placed between the sample and the scintillator. The scintillator was coated with a 20 nm thick layer of aluminum so that it could conduct the emission current and thus be measured.

Because the scintillator can convert the energy of the emitted electrons into photon energy, it was possible to record the emission pattern at different voltages and their corresponding currents. By observing the pattern, it was possible to determine, at least partially quantitatively, which part of the auto-emission pattern is involved in the emission.

The spiral on which the individual emitters are placed is not Fermat, meaning that the individual emitters have different distances from each other. The emitters at the center of the spiral are closer to each other than the emitters at the edge. It can be

observed in the FEM images that the edges of the structure illuminate more intensely at the edges. This may be caused by the fact that the emitters in the center have smaller distances between each other and, therefore, there is a stronger shielding effect.

The I-V characteristic was measured and showed a high onset field with an onset emission current of approximately 130 nA occurring at a voltage of approximately 2.3 kV. When the voltage value of 2.7 kV is exceeded, the emission current becomes stable and in the order of microampere units. The I-V characteristic is exponential. A Murphy-Good plot was constructed which made it possible to analyze the field emission data. An orthodoxy test was applied to this plot, which showed that it was possible to safely measure up to a current value of 24 μ A. Once this value is exceeded the sample surface is destroyed and it is no longer possible to determine the origin of the emission. The parameters characterizing the emitters can be obtained from the Murphy-Good plot, such as the formal emission area $A_f^{SN} = 5.93 \mu\text{m}^2$, the voltage conversion length as $\epsilon = 407 \text{ nm}$, and the field enhancement factor $\gamma = 368.14$ for the Pass region. For Inconclusive region, the parameters are the formal emission area $A_f^{SN} = 0.37 \mu\text{m}^2$, the voltage conversion length as $\epsilon = 3.51 \text{ nm}$, and the field enhancement factor $\gamma = 427.91$.

Lastly, the current stability was measured overtime for 40,000 ms for three different voltages, the data were fitted with a normal distribution which showed that 95 % of the values of the measured current are in the range of no more than 140 nA, which is a very small interval and the current is therefore stable.

The future goals of this work are to adjust the setup of the field emission microscope so that the cathode and the anode are as close to each other as possible so that a high onset field in the order of kilovolts would not be necessary. The next target is to perform multiple measurements on several samples with different numbers of emitters to determine what part of the emission structure participates in the emission the most and to perform current stability measurements on the order of hours to determine how long the structure can operate without disturbing the sample surface.

REFERENCES

- [1] Luo, Y.; Tang, Y.; Chung, T. F.; et al.: Electron work function: an indicative parameter towards a novel material design methodology. *Scientific Reports*, vol. 11, 1, 2021: p. 1–13, ISSN 20452322, doi:[10.1038/s41598-021-90715-4](https://doi.org/10.1038/s41598-021-90715-4).
- [2] Pierret, R. F.: Semiconductor Device Fundamentals. *New York*, 1996, ISSN 0342-1791.
- [3] Kittel, C.: Introduction to Solid State Physics, 8th edition. *Wiley & Sons, New York, NY*, 2004.
- [4] Brodie, I.; Schwoebel, P. (editors): *Field Electron Emission from Metals*. Boston, MA: Springer US, 2005, ISBN 978-0-387-27419-5, p. 1–17, doi:[10.1007/0-387-27419-7_1](https://doi.org/10.1007/0-387-27419-7_1).
- [5] Eckertová, L.; Frank, L.: *Metody analýzy povrchů: elektronová mikroskopie a difrakce*. Praha: Academia, 1. ed., 1996, 379 p.
- [6] Stratton, R.: Field Emission from Semiconductors. *Proceedings of the Physical Society. Section B*, vol. 68, 10, oct 1955: p. 746–757, doi:[10.1088/0370-1301/68/10/307](https://doi.org/10.1088/0370-1301/68/10/307).
- [7] Thomas, R. N.; Wickstrom, R. A.; Schroder, D. K.; et al.: Fabrication and some applications of large-area silicon field emission arrays. *Solid State Electronics*, vol. 17, 2, 1974: p. 155–163, ISSN 00381101, doi:[10.1016/0038-1101\(74\)90063-X](https://doi.org/10.1016/0038-1101(74)90063-X).
- [8] Ding, M.; Sha, G.; Akinwande, A. I.: Silicon field emission arrays with atomically sharp tips: Turn-on voltage and the effect of tip radius distribution. *IEEE Transactions on Electron Devices*, vol. 49, 12, 2002: p. 2333–2342, ISSN 00189383, doi:[10.1109/TED.2002.805230](https://doi.org/10.1109/TED.2002.805230).
- [9] Jensen, K. L.; Shiffler, D. A.; Rittersdorf, I. M.; et al.: Discrete space charge affected field emission: Flat and hemisphere emitters. *Journal of Applied Physics*, vol. 117, 19, May 2015: 194902, doi:[10.1063/1.4921186](https://doi.org/10.1063/1.4921186).
- [10] Spindt, C. A.: A thin-film field-emission cathode. *Journal of Applied Physics*, vol. 39, 7, 1968: p. 3504–3505, ISSN 00218979, doi:[10.1063/1.1656810](https://doi.org/10.1063/1.1656810).

- [11] Spindt, C. A.; Holland, C. E.; Stowell, R. D.: Field emission cathode array development for high-current-density applications. *Applications of Surface Science*, vol. 16, 1-2, 1983: p. 268–276, ISSN 03785963, doi:[10.1016/0378-5963\(83\)90073-9](https://doi.org/10.1016/0378-5963(83)90073-9).
- [12] Lee, H.; Huang, R.: Simulation and design of field emitter array. *IEEE Electron Device Letters*, vol. 11, 12, 1990: p. 579–581, doi:[10.1109/55.63045](https://doi.org/10.1109/55.63045).
- [13] McGruer, N. E.; Warner, K.; Singhal, P.; et al.: Oxidation-Sharpended Gated Field Emitter Array Process. *IEEE Transactions on Electron Devices*, vol. 38, 10, 1991: p. 2389–2391, ISSN 15579646, doi:[10.1109/16.88531](https://doi.org/10.1109/16.88531).
- [14] Jonnson, S.; Markwitz, A.; Rudolphi, M.; et al.: Field emission properties of self-assembled silicon nanostructures on n- and p-type silicon. *Applied Physics Letters*, vol. 85, 15, 2004: p. 3277–3279, ISSN 00036951, doi:[10.1063/1.1804604](https://doi.org/10.1063/1.1804604).
- [15] Harris, J. R.; Jensen, K. L.; Shiffler, D. A.; et al.: Shielding in ungated field emitter arrays. *Applied Physics Letters*, vol. 106, 20, 2015: p. 201603, doi:[10.1063/1.4921709](https://doi.org/10.1063/1.4921709).
- [16] Bieker, J.; Forbes, R. G.; Wilfert, S.; et al.: Simulation-Based Model of Randomly Distributed Large-Area Field Electron Emitters. *IEEE Journal of the Electron Devices Society*, vol. 7, 2019: p. 997–1006, doi:[10.1109/JEDS.2019.2940086](https://doi.org/10.1109/JEDS.2019.2940086).
- [17] Edler, S.; Schels, A.; Herdl, F.; et al.: Origin of the current saturation level of p-doped silicon field emitters. *Journal of Vacuum Science & Technology B*, vol. 40, 1, 2022: p. 013203, doi:[10.1116/6.0001554](https://doi.org/10.1116/6.0001554).
- [18] Fowler, R. H.; Nordheim, L. W.: Electron Emission in Intense Electric Fields. *Proceedings of The Royal Society A: Mathematical, Physical and Engineering Sciences*, vol. 119: p. 173–181.
- [19] Ravipati, S.; Kuo, C. J.; Shieh, J.; et al.: Fabrication and enhanced field emission properties of novel silicon nanostructures. *Microelectronics Reliability*, vol. 50, 12, 2010: p. 1973–1976, ISSN 00262714, doi:[10.1016/j.microrel.2010.06.005](https://doi.org/10.1016/j.microrel.2010.06.005).
- [20] Horacek, M.; Meluzin, P.; Kratky, S.; et al.: Phyllotactic arrangements of optical elements. *Holography: Advances and Modern Trends V*, vol. 10233, 2, 2017: p. 102331G, ISSN 1996756X, doi:[10.1117/12.2265835](https://doi.org/10.1117/12.2265835).
- [21] Kolařík, V.; Horáček, M.; Knápek, A.; et al.: Spiral arrangement: From nanostructures to packaging. *Journal of Electrical Engineering*, vol. 70, 1, 2019: p. 74–77, ISSN 13353632, doi:[10.2478/jee-2019-0011](https://doi.org/10.2478/jee-2019-0011).

- [22] Vogel, H.: A better way to construct the sunflower head. *Mathematical Biosciences*, vol. 44, 3, 1979: p. 179–189, ISSN 0025-5564, doi:[https://doi.org/10.1016/0025-5564\(79\)90080-4](https://doi.org/10.1016/0025-5564(79)90080-4).
- [23] Chrostowski, L.; Shoman, H.; Hammood, M.; et al.: Silicon Photonic Circuit Design Using Rapid Prototyping Foundry Process Design Kits. *IEEE Journal of Selected Topics in Quantum Electronics*, vol. 25, 5, 2019: p. 1–26, doi:[10.1109/JSTQE.2019.2917501](https://doi.org/10.1109/JSTQE.2019.2917501).
- [24] Rinke, T.; Koch, C.; GmbH, M.: *Photolithography: Basics of Microstructuring*. MicroChemicals, 2017.
- [25] Matějka, F.: *Praktická elektronová litografie*. Ústav přístrojové techniky AV ČR, v. v. i., Královopolská 147, CZ–612 64 Brno, 2012.
- [26] Nguyen, K. N.; Basset, P.; Marty, F.; et al.: On the optical and morphological properties of microstructured Black Silicon obtained by cryogenic-enhanced plasma reactive ion etching. *Journal of Applied Physics*, vol. 113, 19, 2013: p. 1–9, ISSN 00218979, doi:[10.1063/1.4805024](https://doi.org/10.1063/1.4805024).
- [27] Toer, P.; Reimer, L.; MacAdam, D.; et al.: *Scanning Electron Microscopy: Physics of Image Formation and Microanalysis*. Springer Series in Optical Sciences, Springer, 1998.
- [28] Stevie, F. A.; Donley, C. L.: Introduction to x-ray photoelectron spectroscopy. *Journal of Vacuum Science & Technology A*, vol. 38, 6, 2020: p. 063204, doi:[10.1116/6.0000412](https://doi.org/10.1116/6.0000412).
- [29] Lecoq, P.: *Scintillation Detectors for Charged Particles and Photons*. Cham: Springer International Publishing, 2020, ISBN 978-3-030-35318-6, p. 45–89, doi:[10.1007/978-3-030-35318-6_3](https://doi.org/10.1007/978-3-030-35318-6_3).
- [30] Allaham, M.; Forbes, R.; Knápek, A.; et al.: Implementation of the Orthodoxy Test as a Validity Check on Experimental Field Emission Data. *Journal of Electrical Engineering*, vol. 71, 03 2020: p. 37–42, doi:[10.2478/jee-2020-0005](https://doi.org/10.2478/jee-2020-0005).
- [31] Madanat, M.; Al Share, M.; Allaham, M. M.; et al.: Information extraction from Murphy–Good plots of tungsten field electron emitters. *Journal of Vacuum Science & Technology B*, vol. 39, 2, 2021: p. 024001, doi:[10.1116/6.0000803](https://doi.org/10.1116/6.0000803).

LIST OF ABBREVIATIONS

GDS	Graphic Design System
OASIS	Open Artwork System Interchange Standard
GUI	Graphical User Interface
PCell	Parameterized Cell
HMDS	Hexamethyldisilazane
PEB	Post-Exposure Bake
BOE	Buffered Oxide Etch
RIE	Reactive Ion Etching
DRIE	Deep Reactive Ion Etching
b-Si	Black Silicon
ICP	Inductively Coupled Plasma
HF	High Frequency
SCCM	Standard Cubic Centimeters per Minute
SEM	Scanning Electron Microscope
FEM	Field Emission Microscope
XPS	X-ray Photoelectron Spectroscopy
BE	Binding Energy
KE	Kinetic Energy
FEA	Field Emitter Array
UPS	Ultraviolet Photoelectron Spectroscopy
M-G	Murphy-Good

S-N Schottky–Nordheim

VLC Voltage Conversion Length